



Article

<https://doi.org/10.1038/s42255-024-01082-z>

Non-invasive mapping of brown adipose tissue activity with magnetic resonance imaging

Received: 22 August 2023

Accepted: 14 June 2024

Published online: 25 July 2024

Zimeng Cai^{1,2,3,18}, Qiaoling Zhong^{4,18}, Yanqiu Feng^{5,6,7,18}, Qian Wang^{8,18}, Zuoman Zhang⁹, Cailv Wei¹⁰, Zhinan Yin¹⁰, Changhong Liang^{1,3}, Chong Wee Liew¹⁰, Lawrence Kazak¹⁰, Aaron M. Cypess¹⁰, Zaiyi Liu^{1,3}✉ & Kejia Cai^{16,17}

Check for updates

Thermogenic brown adipose tissue (BAT) has a positive impact on whole-body metabolism. However, *in vivo* mapping of BAT activity typically relies on techniques involving ionizing radiation, such as [¹⁸F]fluorodeoxyglucose ([¹⁸F]FDG) positron emission tomography (PET) and computed tomography (CT). Here we report a noninvasive metabolic magnetic resonance imaging (MRI) approach based on creatine chemical exchange saturation transfer (Cr-CEST) contrast to assess *in vivo* BAT activity in rodents and humans. In male rats, a single dose of the β_3 -adrenoceptor agonist (CL 316,243) or norepinephrine, as well as cold exposure, triggered a robust elevation of the Cr-CEST MRI signal, which was consistent with the [¹⁸F]FDG PET and CT data and ¹H nuclear magnetic resonance measurements of creatine concentration in BAT. We further show that Cr-CEST MRI detects cold-stimulated BAT activation in humans (both males and females) using a 3T clinical scanner, with data-matching results from [¹⁸F]FDG PET and CT measurements. This study establishes Cr-CEST MRI as a promising noninvasive and radiation-free approach for *in vivo* mapping of BAT activity.

Obesity prevalence has markedly increased worldwide in recent decades¹. In addition to its specific comorbidities, obesity is a major risk factor for other metabolic conditions, such as insulin resistance, type 2 diabetes (T2D) mellitus, cardiovascular diseases and certain types of cancer^{2–4}. Obstacles to treating these metabolic diseases are a major global challenge^{5,6}. It is noteworthy that activation of thermogenic brown and beige adipocytes⁷ has the potential to be a safe strategy to treat obesity-related metabolic disease^{8–10}. Both cold exposure and pharmacological adrenergic receptor activation trigger energy dissipation of existing thermogenic adipocytes in brown adipose tissue (BAT) and convert white adipocytes and adipocyte precursor cells into beige thermogenic adipocytes^{11,12}.

Non-shivering thermogenesis through UCP1 is a major mechanism of BAT-mediated energy expenditure¹³. However, additional

futile cycles dependent on ATP synthesis and consumption promote energy dissipation in a UCP1-independent manner, such as the futile lipid^{14–17}, creatine^{18–21} and calcium cycles²². Creatine is also linked to mitochondrial metabolism and has an important role in the process of mitochondrial oxidative phosphorylation. Therefore, the role of creatine in energy-intensive tissues with a highly variable respiratory rate, and its links to ATP-linked thermogenesis, suggest that creatine could represent a potential biomarker for BAT metabolic function and the diagnosis and treatment of metabolic diseases.

Understanding thermogenic signal pathways and then using them to develop treatments necessitate the development of noninvasive imaging and monitoring methods. Currently, ¹⁸F-fluorodeoxyglucose (¹⁸F-FDG) positron emission tomography (PET) and computed tomography (CT) is the most commonly used method for detecting and

A full list of affiliations appears at the end of the paper. ✉ e-mail: liuzaiyi@gdph.org.cn

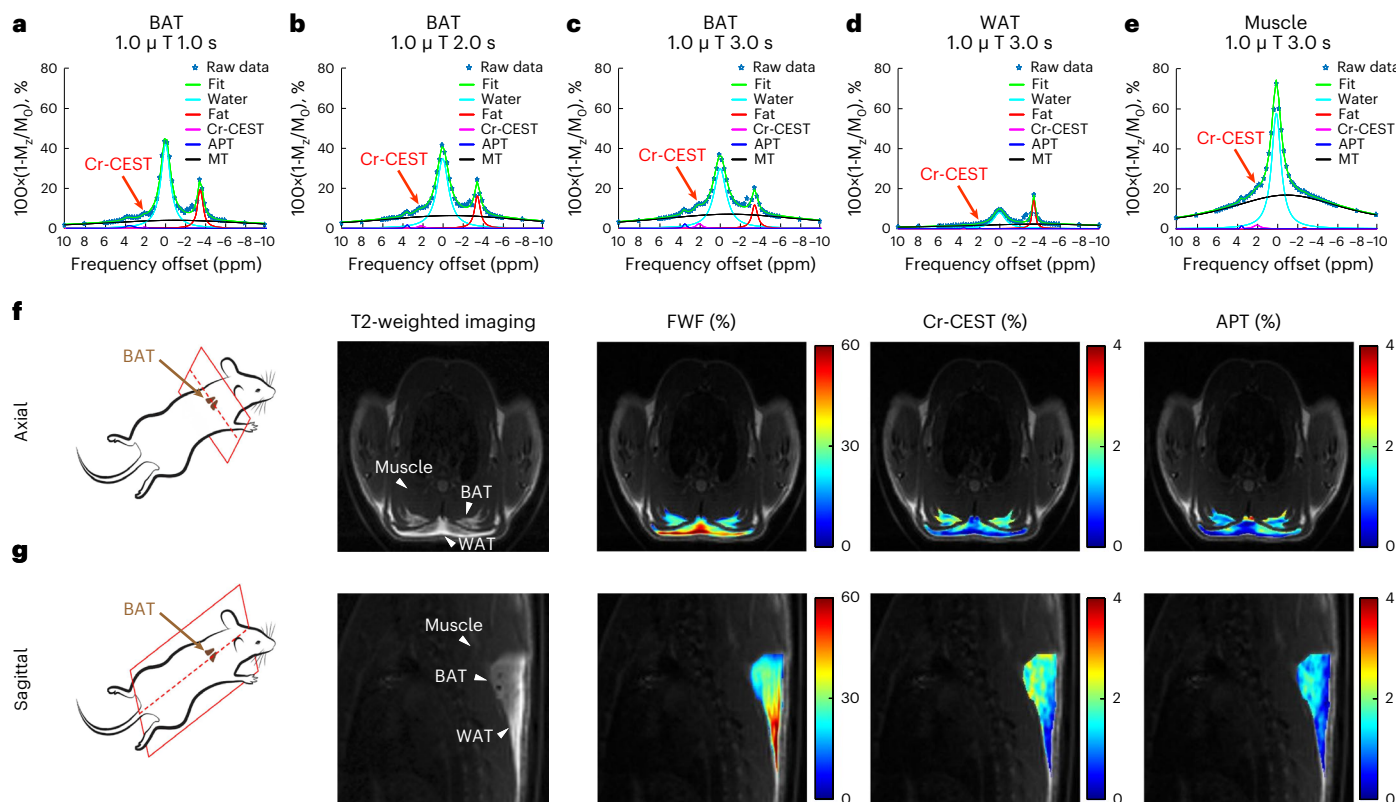


Fig. 1 | Z-spectral fitting of adipose tissues producing multi-parametric contrasts including Cr-CEST. **a–c**, Fitting of the Z-spectra of BAT under different pre-saturation durations: 1.0 μ T for 1.0 s (**a**), 2.0 s (**b**) and 3.0 s (**c**). The Cr-CEST peaks (red arrows) could be observed visually. **d,e**, Z-spectra of WAT (**d**) and muscle (**e**) under a 1.0 μ T saturation for 3.0 s. **f,g**, Demonstration of the selection

of image slices from the axial (**f**) and sagittal (**g**) views of rats' interscapular fat depots, representative structural T2-weighted images and the corresponding FWF, Cr-CEST and APT maps obtained from the Z-spectral fitting. Representative image from $n = 6$. In the T2-weighted images, the arrowheads point to the BAT, WAT and muscle regions, respectively.

quantifying BAT metabolic activity in humans^{23,24}. However, radiation exposure and the pharmacodynamic profile of PET tracers limit the use of PET and CT in longitudinal imaging²⁵. Furthermore, [¹⁸F]FDG uptake is fully maintained even when oxygen consumption and adipocyte thermogenesis are diminished, suggesting that increased BAT [¹⁸F]FDG uptake may occur independently of thermogenesis²⁶. On the other hand, magnetic resonance imaging (MRI) displays superior soft tissue contrast and uses only non-ionizing radiation, making it an ideal imaging candidate for longitudinal studies²⁷. Most currently available MRI techniques are designed for studying structural information of adipose tissues, such as Dixon's MRI used for mapping fat-water fraction (FWF). There is no endogenous MRI that is sensitive to the metabolic function of adipose tissues.

Chemical exchange saturation transfer (CEST) MRI is an emerging noninvasive and endogenous metabolic imaging technique that detects tissue metabolites that exchange protons with water, such as those having amine (-NH₂), amide (-NH), hydroxyl (-OH) or sulphydryl (-SH) groups. By collecting high-resolution CEST-weighted images at a range of saturation frequency offsets, a Z-spectrum is formed^{28,29}. Depending on the abundance of CEST-expressing metabolites in tissue, the exchange rate and the frequency offset of their exchanging protons, CEST MRI is capable of noninvasively imaging proteins³⁰, liver glycogen³¹, cartilage glycosaminoglycans³² and brain glutamate³³ with a spatial resolution down to the submillimetre range.

Based on its exchangeable guanidinium protons, creatine CEST (Cr-CEST) MRI has been developed and investigated in several tissues, including brain³⁴, tumours^{35,36}, heart³⁷ and calf muscles^{38,39}. As BAT exhibits creatine kinase activity within the same order of magnitude as cardiac or nerve tissue⁴⁰, our goal in this study was to

develop Cr-CEST MRI to image the metabolic function of adipose tissues. Cr-CEST MRI for BAT function was validated in animals receiving BAT-activating drugs and then in humans exposed to cold, along with independent PET and CT scans and biochemical measurements. Moreover, the fat signal has been historically treated as an artefact in CEST Z-spectra and researchers have struggled to suppress or remove it^{41,42}. We take the opposite and innovative strategy to keep both the fat and Cr-CEST signals in Cr-CEST MRI simultaneously, realizing the combination of fat content and adipocyte metabolic function imaging.

Results

Observation and quantification of Cr-CEST from Z-spectra

We acquired Z-spectra, that is, plots of water signal attenuation versus off-resonance saturation frequency, from the rat interscapular fat depot with 1.0 μ T saturation power and varied saturation durations (1.0 s, 2.0 s and 3.0 s) on a small-bore horizontal 7T MRI scanner. Relatively low saturation power (1.0 μ T) was used for better visualization of any CEST effect from Z-spectra. Z-spectral images (M_z) with several frequency offsets ranging from -10 to +10 ppm were normalized using a reference image (M_0) at +300 ppm and corrected for B_0 inhomogeneities by shifting the dip of water direct saturation to 0 ppm. The reversed pixel-wise raw Z-spectral data ($1-M_z/M_0$, blue stars) were then fitted with multicomponent Lorentzian functions (Fig. 1a–e), corresponding to the peak of water direct saturation (cyan line, centred at 0 ppm), the main methylene fat direct saturation peak (red line, centred at -3.5 ppm), the CEST peak observed at around +2 ppm (Cr-CEST, purple line), the amide proton transfer (APT) effect (blue line, centred at +3.5 ppm) and the broadband semi-solid magnetization transfer (MT) effect (black line,

Table 1 | Initial values and fitting constraints for the frequency offsets, line widths and amplitudes of the five main components contributing to Z-spectra in both rats and humans under all conditions

Parameters	Initial values (lower and upper limit)				
	Water	Fat or lipid	Semi-solid MT	Cr-CEST ^a	APT ^a
Frequency offset, ppm	0 (-0.5 to 0.5)	-3.4 (-4.0 to -3.0)	-1.5 (-4 to -1)	2.0 (1.6 to 2.4)	3.5 (3.0 to 4.0)
Line width, ppm	2.0 (0.1 to 10)	1.0 (0.1 to 5)	50 (20 to 100)	0.5 (0.1 to 5)	0.5 (0.1 to 5)
Amplitude, %	40 (0.01 to 100)	15 (0.01 to 100)	10 (0.01 to 40)	2 (0.01 to 20)	2 (0.01 to 20)

^aCr-CEST and APT peaks were refitted in a secondary fitting procedure after removing the three major signals of water, fat and MT.

centred between -1 to +1 ppm). The fitting produced several contrast maps, including FWF, Cr-CEST and APT maps (Table 1). The FWF was quantified as the peak amplitude of the methylene fat divided by the sum of the fat and water amplitudes. BAT and white adipose tissue (WAT) in the interscapular fat depot can be visually differentiated in T2-weighted images (Fig. 1f,g).

We consistently observed a CEST peak at approximately 2 ppm in the Z-spectra of BAT at all saturation durations. According to the literature, the CEST at 2 ppm peak is attributed to creatine^{35,43} and the 3.5 ppm peak to the APT effect from mobile proteins and peptides^{44,45}, which is also visible in BAT Z-spectra. The fitted Cr-CEST peak increased with saturation duration (red arrows, Fig. 1a–c). Therefore, we chose 3.0 s for the rest of the Cr-CEST imaging studies. Compared with BAT, WAT had a lower water signal (Fig. 1d) and muscle tissue had a higher water signal (Fig. 1e), as expected. BAT had higher Cr-CEST and APT signals than WAT (Fig. 1f,g).

Imaging of BAT activation with Cr-CEST and [¹⁸F]FDG PET

The selective β_3 -adrenergic receptor agonist CL 316,243 (CL) activated BAT thermogenesis in rodents⁴⁶. To investigate whether Cr-CEST imaging can detect BAT activation, we injected rats with a single intraperitoneal dose of saline or CL (1.0 mg kg⁻¹ body weight) and performed dynamic Cr-CEST imaging of the interscapular fat at a 10-min interval for up to 2 h after the injection. For validation, a separate group of rats receiving the same dose of saline or CL was scanned with [¹⁸F]FDG PET.

For rats receiving only saline, the dynamic Cr-CEST signals of BAT ($0.80 \pm 0.21\%$) and WAT ($0.25 \pm 0.16\%$) were relatively stable after the injection with saline (Fig. 2a,b). There was no difference in FDG uptake between BAT and WAT due to saline; the mean standard uptake value (SUV_{mean}) of both BAT and WAT increased rapidly after FDG injection and then gradually decreased to a relatively stable value (Fig. 2c,d), reflecting the pharmacodynamics of [¹⁸F]FDG.

We can directly observe from the Z-spectrum that only BAT showed obvious changes after CL administration, that is, an increase in the Cr-CEST signal, accompanied by an increase in the water signal and a decrease in the fat signal, indicating a decrease in FWF during BAT activation (Extended Data Fig. 1). What is more, we did not observe any significant changes in WAT using either Cr-CEST MRI (Fig. 2e,f) or PET and CT imaging (Fig. 2g,h). In contrast, the Cr-CEST from BAT increased significantly within 20 min from $0.56 \pm 0.23\%$ to $1.96 \pm 0.31\%$ and plateaued for the remaining 2 h after the injection (Fig. 2e,f). Similarly, the FDG uptake in BAT over 2 h in the [¹⁸F]FDG PET and CT experiments increased continuously (Fig. 2g,h).

Next, a separate group of rats was used to examine CL-mediated creatine changes with ¹H-nuclear magnetic resonance (¹H-NMR). The creatine concentration in BAT measured with ¹H-NMR showed a significant increase within 20 min after the injection with CL (Fig. 2i) and was well correlated with Cr-CEST MRI across different time points (Fig. 2j). CL administration triggered an increase in thermogenic gene expression, including Dio2, Ppargc1 α , Ckb and Ucp1 (Fig. 2k–n). In addition, the injection with CL triggered a rise in the oxygen consumption of rats within 20 min, which was sustained for 2 h, and matched well with the

Cr-CEST results (Fig. 2f,o), indicating that Cr-CEST is closely related to pharmacological BAT activation.

Effect of norepinephrine activation on BAT detection using Cr-CEST and [¹⁸F]FDG PET

Unlike CL, which stimulates rodent BAT activity via the selective β_3 -adrenergic receptor agonist, norepinephrine (NE) targets both α -adrenergic and β -adrenergic receptors⁴⁷. We tested whether NE-stimulated BAT activation could also be detected with Cr-CEST MRI. After NE administration (1.0 mg kg⁻¹), we directly observed from the Z-spectrum that only BAT showed obvious changes (Extended Data Fig. 2), which is consistent with the previous stimulation with CL (Extended Data Fig. 1). Furthermore, the Cr-CEST from BAT increased significantly within 20 min from $0.56 \pm 0.16\%$ to $2.29 \pm 0.29\%$ and was significantly high for 2 h after the injection (Fig. 3a,b). Similarly, the creatine concentration in BAT, measured with ¹H-NMR, significantly increased within 20 min after NE administration (Fig. 3g) and correlated well with Cr-CEST at different time points (Fig. 3h). Like CL, NE treatment increased the mRNA expression of thermogenic genes, such as Dio2, Ppargc1 α , Ckb and Ucp1 (Fig. 3i–l). In addition, the trend of oxygen consumption rate (OCR) in rats after NE stimulation agreed with the Cr-CEST results; both increased within 20 min and gradually decreased in the later stage (Fig. 3b,m). The transient nature of NE is probably due to its metabolism in vivo, and possibly because of its lower lipolytic action compared to CL⁴⁸.

However, in the PET and CT experiment, the SUV_{mean} value of BAT was low for 2 h after the injection with 1.0 mg kg⁻¹ NE (Fig. 3c,d). Only by increasing the NE dose to 2.5 mg kg⁻¹, the SUV_{mean} value of BAT significantly increased and lasted for 2 h (Fig. 3e,f), indicating the higher sensitivity of Cr-CEST MRI compared with [¹⁸F]FDG PET and CT in detecting BAT activation.

Improving the resolution of Cr-CEST imaging (from an in-plane resolution of 0.312×0.312 mm² to 0.156×0.156 mm²), despite a longer imaging time (from 8 to 16 min), reduced the partial volume effect and clearly delineated the boundaries between BAT and WAT (Extended Data Fig. 3). Multi-slice Cr-CEST MRI covering the entire rat interscapular fat depot were also demonstrated 30 min after NE stimulation (Extended Data Fig. 4).

Cr-CEST detects BAT adrenergic activation in cold-exposed rats

Cold exposure activates BAT thermogenesis⁴⁹. Individual rats were placed in precooled cages without bedding at 4 °C for 2 h. The results of the BAT Cr-CEST signal at room temperature and after 2 h of acute cold exposure (4 °C) are shown in Fig. 4 and Extended Data Fig. 5. In response to cold exposure, the Z-spectrum of muscle showed a slightly increased Cr-CEST signal, while BAT showed significantly increased water and Cr-CEST signal and decreased fat signal; WAT showed no difference before and after cold exposure (Extended Data Fig. 5). The dynamic Cr-CEST in rat muscle was stable due to drugs (Extended Data Figs. 1 and 2); it showed a small increase after cold exposure (Extended Data Fig. 5), indicating that cold exposure in rats induced a small thermogenic effect in muscle also. BAT Cr-CEST increased significantly from $0.71 \pm 0.27\%$

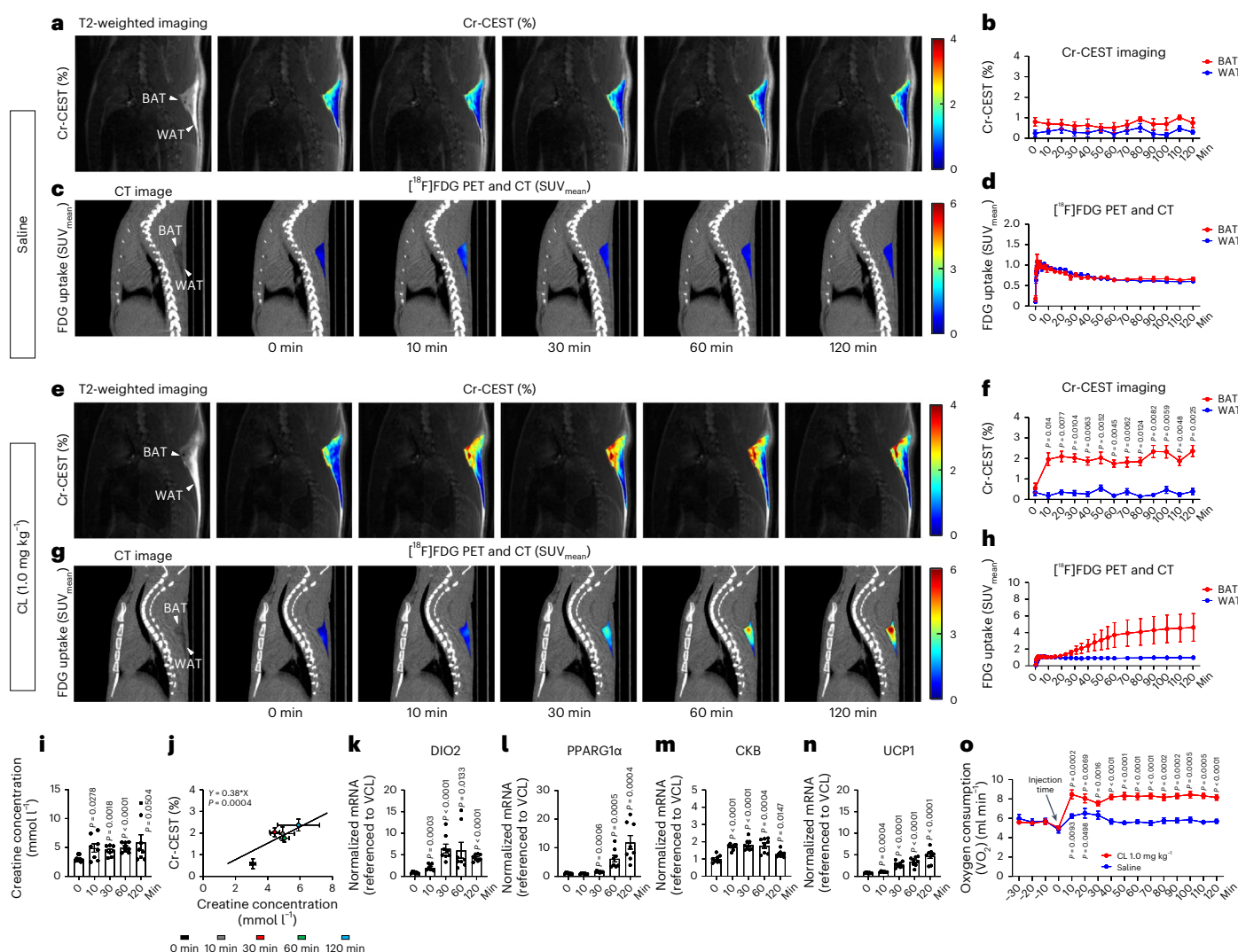


Fig. 2 | Dynamic Cr-CEST MRI and [¹⁸F]FDG PET and CT detect the response to saline and the β_3 -adrenergic receptor agonist CL. **a–d**, Dynamic Cr-CEST MRI ($n = 6$) and [¹⁸F]FDG PET and CT ($n = 4$) of interscapular fat depots after intraperitoneal injection with saline in rats: representative images (Cr-CEST % (a), FDG uptake SUV (c)) and signals (Cr-CEST % (b), FDG uptake SUV_{mean} (d)). Representative image from $n = 6$ in Cr-CEST MRI and $n = 4$ in [¹⁸F]FDG PET and CT. **e–h**, Dynamic Cr-CEST MRI ($n = 6$) and [¹⁸F]FDG PET and CT ($n = 3$) of interscapular fat depots after intraperitoneal injection with CL (1.0 mg kg⁻¹) in rats: representative images (Cr-CEST % (e), FDG uptake SUV_{mean} (g)) and signals (Cr-CEST % (f), FDG uptake SUV_{mean} (h)). Representative image from $n = 6$ in Cr-CEST MRI and $n = 3$ in [¹⁸F]FDG PET and CT. **i**, **j**, H-NMR analysis of

BAT creative concentration; the creative concentration of BAT increased after the administration of CL (1.0 mg kg⁻¹, $n = 8$, a separate cohort from **f**). **j**, Linear regression analysis of Cr-CEST MRI in relation to creative concentration (cohorts in **i**, **j**). **k–n**, Real-time PCR analysis of thermogenesis-related gene expression due to CL (1.0 mg kg⁻¹) in the BAT of rats; all experiments were repeated at least twice with similar results ($n = 8$). **k**, DIO2. **l**, PPARG1 α . **m**, CKB. **n**, UCP1. **o**, Dynamic OCR of rats under saline ($n = 6$) or CL ($n = 8$) stimulation. Data are presented as the mean \pm s.e.m. Statistical analysis was performed using two-tailed paired (**f**, **o**) and unpaired (**i**, **k–n**) Student's *t*-tests; each time point (10–120 min) was compared to 0 min (**f**, **i**, **k–n**) and –10 min (**o**), respectively. In the T2-weighted and CT images, the arrowheads indicate the BAT and WAT regions, respectively.

at room temperature to $1.95 \pm 0.25\%$ after exposure to cold (Fig. 4). In contrast, WAT showed no statistically significant differences in Cr-CEST signal between room temperature ($0.36 \pm 0.06\%$) and cold ($0.34 \pm 0.06\%$) (Fig. 4).

Cr-CEST MRI detects cold-activated BAT in humans

To evaluate the feasibility of Cr-CEST imaging of human BAT in a clinical 3T MRI, we performed Cr-CEST MRI and [¹⁸F]FDG PET and CT imaging in healthy individuals exposed to mild cold (Fig. 5). Fifty healthy volunteers (27 men and 23 women) underwent Cr-CEST imaging; from this group, 14 randomly selected individuals (7 men and 7 women) also underwent [¹⁸F]FDG PET and CT imaging. After being exposed to a mild cold temperature for 2 h, the human Z-spectra data showed that only the water and Cr-CEST peaks had significantly

increased signals (Extended Data Fig. 6). Unfortunately, for the human studies using a 3T clinical scanner, because of the broad water direct saturation spectrum affecting the nearby Cr-CEST peak (Extended Data Fig. 6), it was hard to separate the Cr-CEST peak from the water peak. Therefore, fitting the muscle Z-spectrum for consistent and comparable Cr-CEST to the adipose tissues (BAT and WAT) was challenging. Such a task can be better achieved in rats under ultrahigh field 7T MRI, where the water and Cr-CEST peaks are more distinctive (Extended Data Figs. 1, 2 and 5). It is worth noting that the fat peak in human (Extended Data Fig. 6) BAT did not change as much as the fat peak of rats after cold exposure (Extended Data Fig. 5) probably because of the different cold exposure conditions in humans (RT of 16–17 °C and a 6–10 °C cooling vest for 2 h) compared with rats (2 h in climate-controlled cold rooms at 4 °C).

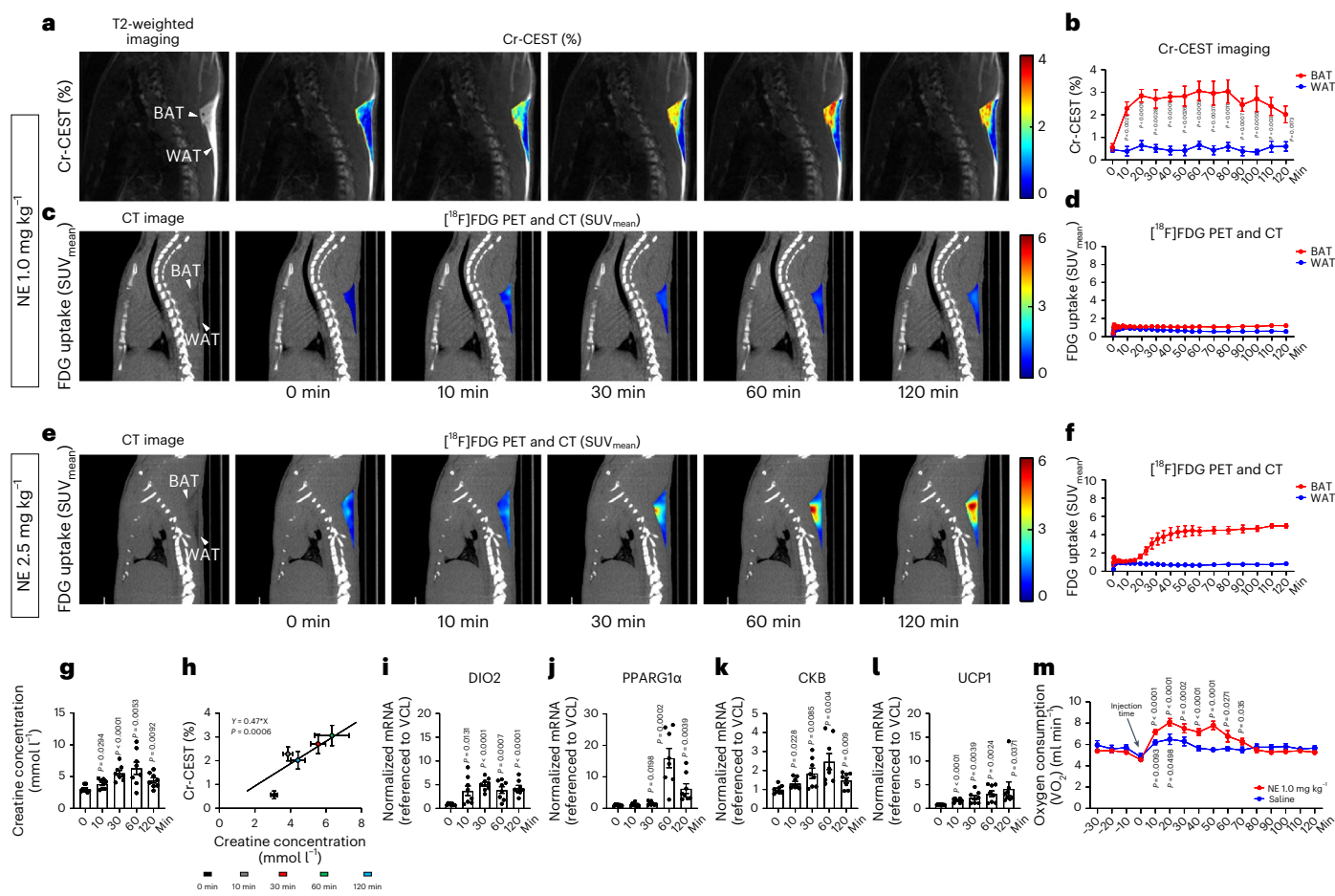


Fig. 3 | Dynamic Cr-CEST MRI detects the response to NE. a–d, Dynamic Cr-CEST MRI ($n = 6$) and [^{18}F]FDG PET and CT ($n = 4$) of interscapular fat depots after intraperitoneal injection with NE (1.0 mg kg^{-1}) in rats: representative images (Cr-CEST % (a), FDG uptake SUV_{mean} (c)) and signals (Cr-CEST % (b), FDG uptake SUV_{mean} (d)). Representative image from $n = 6$ in Cr-CEST MRI and $n = 4$ in [^{18}F]FDG PET and CT. e,f, Dynamic [^{18}F]FDG PET and CT ($n = 3$) of interscapular fat depots after intraperitoneal injection with NE (1.0 mg kg^{-1}) in rats: representative images (FDG uptake SUV_{mean} (e)) and signals (FDG uptake SUV_{mean} (f)). g, ^1H -NMR analysis of BAT creatine concentration. The creatine concentration of BAT increased after the administration of NE (1.0 mg kg^{-1} , $n = 8$, separate cohort from b). h, Linear

regression analysis of Cr-CEST MRI in relation to creatine concentration (cohorts in b,g). i–l, Real-time PCR analysis of thermogenesis-related gene expression due to NE (1.0 mg kg^{-1}) in the BAT of rats; all experiments were repeated at least twice with similar results ($n = 8$). m, Dynamic OCR of rats under saline ($n = 6$) or NE ($n = 8$) stimulation. Data are presented as the mean \pm s.e.m. The statistical analysis was performed using two-tailed paired (b,m) and unpaired (g,i–l) Student's *t*-tests; each time point (10–120 min) was compared to 0 min (b,g,i–l) and –10 min (m), respectively. In the T2-weighted and CT images, the arrowheads indicate the BAT and WAT regions, respectively.

Cr-CEST in the supraclavicular BAT increased from $1.44 \pm 0.09\%$ at room temperature to $1.84 \pm 0.11\%$ after cold exposure (Fig. 6a,b; $P < 0.001$). In contrast, the subcutaneous abdominal WAT Cr-CEST was the same before ($0.41 \pm 0.03\%$) and after ($0.44 \pm 0.03\%$) cold exposure (Fig. 6c). Cr-CEST correlates with body mass index (BMI) at RT; this may explain the variations in Cr-CEST at room temperature (Fig. 6d). The BAT and WAT FDG uptake in humans, as measured using the [^{18}F]FDG PET SUV_{mean}, was consistent with the Cr-CEST MRI (Fig. 6g–i). However, because of the unmatched sample sizes of Cr-CEST ($n = 50$) and [^{18}F]FDG PET ($n = 14$), only a moderate correlation was found between Cr-CEST MRI and [^{18}F]FDG PET (Fig. 6j). In addition, we found no differences in Cr-CEST and its changes between men and women (Fig. 6e–f).

The influence of temperature on the Cr-CEST signal

We investigated the effect of temperature on Cr-CEST imaging using in vitro phantom experiments. Phantoms ($n = 3$ sets) contain vials of creatine with concentrations of 2.5 mM, 5.0 mM, 7.5 mM, 10 mM, 15 mM and 20 mM at pH 7.0. By heating the phantoms with a hot-water pad, we investigated the variation in Cr-CEST signal with temperature, from 35°C to 39°C (Extended Data Fig. 7) as the temperature change in BAT

due to cold exposure was expected to be within 2°C ^{50–52}. Extended Data Fig. 7 shows that only when the concentration of creatine was equal to or higher than 10 mM, the Cr-CEST signal showed an observable tendency to gradually decrease when temperature increased from 35°C to 39°C . With regard to the phantom data, we estimated that the in vivo creatine concentration in BAT is about 2.5 mM before cold exposure and about 5 mM after cold exposure. In addition, the dynamic Cr-CEST in WAT remained stable. All of this indicated that the increases in the BAT Cr-CEST signal due to drugs and cold exposure were not caused by temperature itself.

B₀ and B₁ maps of rats and humans

Before Z-spectral fitting, the B₀ inhomogeneities of Z-spectra were carefully corrected on a pixel-by-pixel basis with regard to the water (0 ppm) and fat (-3.4 ppm) signals in this study. We constructed both Z-spectral fitting-based and WAtter Saturation Shift Referencing (WASSR)-based B₀ maps under different time points after CL (Extended Data Fig. 8a–d); the results showed that two sets of B₀ maps were essentially the same and the difference was smaller than the variations between the dynamic scans.

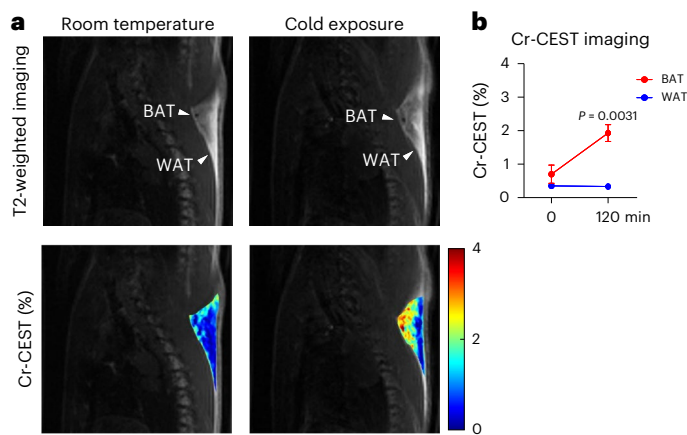


Fig. 4 | Cr-CEST MRI detects BAT adrenergic activation in cold-exposed rats. **a**, Quantitative maps of BAT Cr-CEST at room temperature and under cold exposure. **b**, BAT Cr-CEST increased significantly after a 2-h cold exposure, while WAT Cr-CEST showed no significant difference before and after cold exposure. Representative image from $n = 7$. Data were acquired from Cr-CEST imaging ($n = 7$). Data are presented as the mean \pm s.e.m. The statistical analysis was performed using two-tailed paired Student's *t*-tests (**b**). In the T2-weighted images, the arrowheads indicate the BAT and WAT regions, respectively.

B_1 correction for CEST studies is a common challenge in CEST MRI research. Luckily, the B_1 maps of the adipose tissue and muscle areas in rats showed homogeneity, mostly within 10% variations (Extended Data Fig. 8e). For the human study using the 3T clinical MRI, B_0 maps showed good homogeneity in the left and right sides of the body (Extended Data Fig. 9b). Although the B_1 maps showed a difference between the two sides of the body (Extended Data Fig. 9c), the Cr-CEST signals before and after cold exposure and the corresponding Cr-CEST changes showed no statistically significant differences (Extended Data Fig. 9d–f), indicating that this range of B_0 and B_1 variations is acceptable.

Cr-CEST normalized to the total or water signal

By normalizing Cr-CEST to the total signal (the unsaturated signal at +300 ppm containing both water and fat signals) or the water signal (signal of the water peak) before and after cold exposure, Cr-CEST maps showed similar overall spatial patterns of BAT activation (Extended Data Fig. 10a) at different scales. Cr-CEST normalized to the water signal produced higher Cr-CEST values ($5.01 \pm 0.20\%$ at room temperature and $6.16 \pm 0.29\%$ after cold exposure) than when normalized to the total signal ($1.44 \pm 0.09\%$ at room temperature and $1.84 \pm 0.11\%$ after

cold exposure), with a less relative cold-induced increment in BAT ($25.81 \pm 4.80\%$ versus $33.45 \pm 5.30\%$) (Extended Data Fig. 10b).

Normalization of Cr-CEST to the total signal represents the overall creatine concentration in tissue, whereas normalization to the water signal represents the creatine concentration in the intracellular fluid compartments. During the activation of BAT, the water signal increased while the lipid signal decreased. The FWF changed, while the total signal was relatively constant and was a better denominator than the water signal alone. Compared to the normalization of the total signal, the normalization of the water signal produced higher Cr-CEST values, but a lower relative cold-induced increment in BAT.

Discussion

The principal physiological function of rodents and human BAT is thermogenesis. In the process of BAT thermogenesis, creatine, as one of the metabolites directly involved in ATP recycling, has an important role in ATP-based futile cycling. Creatine promotes the release of a molar excess of ADP from mitochondria⁴⁶, which in turn promotes ATP regeneration, substrate oxidation and thermogenesis^{13,20,53}. Therefore, we posited that creatine may serve as a biomarker for the metabolic function of adipose tissue. In this study, we demonstrated the feasibility of Cr-CEST MRI for noninvasive and functional imaging of adipose tissues to detect BAT activation *in vivo*. Dynamic Cr-CEST detected BAT adrenergic activation in rats in response to CL and NE injections or cold exposure, validated with [¹⁸F]FDG PET and CT and biochemical measurement of creatine concentration, as well as thermogenic gene expression and the monitoring of energy expenditure. Cr-CEST MRI also detected cold-induced BAT activation in humans, consistent with [¹⁸F]FDG PET and CT imaging.

CEST MRI of creatine kinase metabolites—creatinine, phosphocreatine (PCr), ATP and ADP—was explored⁵⁴ and displayed predominant CEST contrast from creatine at 2 ppm with negligible contributions from PCr, ATP and ADP. CEST detection of PCr is challenging and only feasible at the ultrahigh field from 9.4 to 21T^{55–58}, probably because of its slow proton exchange rate (140 ± 60 per s)⁵⁴. Unlike PCr, creatine usually has a relatively high exchange rate (950 ± 100 per s)⁵⁴, making *in vivo* Cr-CEST more favourable. Cr-CEST MRI has a detection sensitivity a hundred times higher than ¹H-MR spectroscopy (¹H-MRS), enabling high-resolution imaging of creatine^{37–39}. Cr-CEST MRI has been used to image several bioenergetic pathologies associated with tumour-bearing brains³⁵, hearts³⁷ and calf muscles^{38,39}. In this study, we used Cr-CEST MRI for the functional imaging of fat tissues.

Activation of BAT thermogenesis with adrenergic receptor stimulation was accompanied by an increase in dynamic Cr-CEST contrast. We observed similar spatial distributions of Cr-CEST and FDG PET signals during BAT activation in rats due to CL or NE administration,

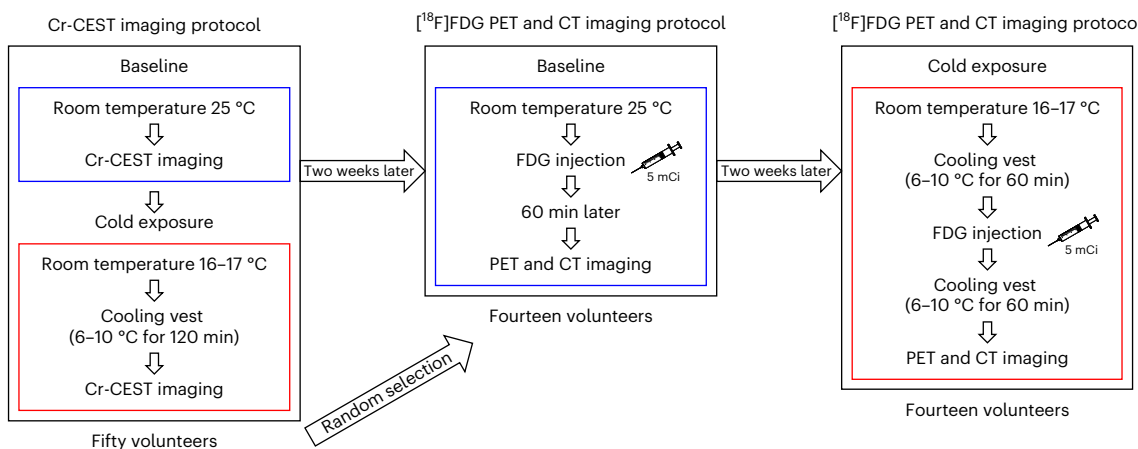


Fig. 5 | Flowchart of the human studies at room temperature (baseline) and after cold exposure. Fourteen individuals were randomly selected for PET and CT imaging from 50 healthy volunteers selected for Cr-CEST imaging.

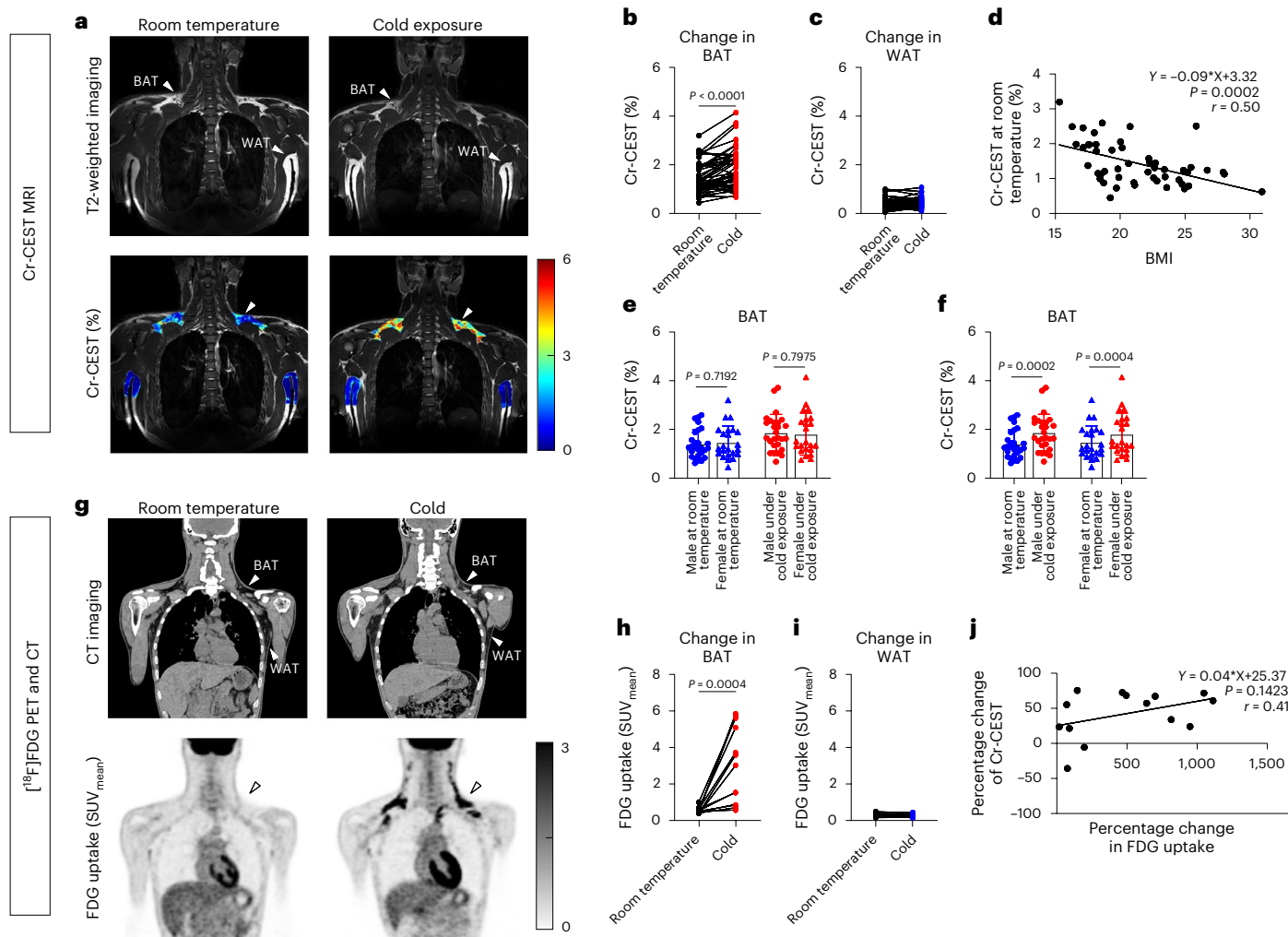


Fig. 6 | Cr-CEST MRI detects BAT adrenergic activation in cold-exposed humans. **a**, Representative Cr-CEST maps for both the BAT and WAT regions in humans before and after cold exposure. **b**, BAT Cr-CEST increased significantly after a 2-h cold exposure. **c**, WAT Cr-CEST showed no difference before and after cold exposure. **d**, Linear regression analysis of resting-state Cr-CEST MRI in relation to BMI. **e**, Under the same experimental conditions (room temperature or cold exposure), there was no statistical difference in BAT Cr-CEST between male ($n = 27$) and female ($n = 23$) volunteers. **f**, BAT Cr-CEST in both male and female volunteers showed the same statistical power before and after cold exposure. **g**, $[^{18}\text{F}]$ FDG PET and CT imaging of interscapular fat depots at room

temperature and under cold exposure. **h,i**, Differences in BAT (h) and WAT (i) FDG uptake before and after cold exposure. **j**, Linear regression analysis on the percentage change of Cr-CEST in relation to FDG uptake using $[^{18}\text{F}]$ FDG PET in volunteers who underwent both Cr-CEST and $[^{18}\text{F}]$ FDG PET imaging ($n = 14$). Representative image from $n = 50$ in Cr-CEST MRI and $n = 14$ in $[^{18}\text{F}]$ FDG PET and CT imaging ($n = 14$). The statistical analysis was performed using two-tailed paired (b,f,h) and unpaired (e) Student's *t*-tests. In the T2-weighted and CT images, the arrowheads indicate the BAT and WAT regions, respectively.

indicating that high-resolution Cr-CEST contrast is consistent with FDG PET and CT imaging. By comparing the time course of dynamic signals, when the FDG signal readout typically requires 30–60 min of tracer uptake, the endogenous Cr-CEST MRI readout does not have such constraints. However, we observed larger variations in dynamic Cr-CEST signals than in FDG PET because of the inevitable motion artefacts in body MRI.

For Cr-CEST validation, *in vivo* ^1H -MRS of creatine is a direct method. However, with high lipid content, adipose tissues have nine peaks on ^1H -MRS (0.9, 1.3, 1.6, 2.02, 2.24, 2.75, 4.1, 4.3 and 5.3 ppm, respectively) when the water proton is at 4.7 ppm. Larger peaks shade the small creatine peak located at approximately 3.0 ppm. Suppression of both water and lipid signals for the quantification of creatine will also suppress the creatine signal, which makes *in vivo* ^1H -MRS of creatine in adipose tissues impractical. Therefore, we validated Cr-CEST with ex vivo ^1H -NMR experiments. To preserve metabolites, tissues were snap-frozen right after dissection. Next, samples were freeze-dried

for at least 36 h in a SpeedVac before they were homogenized and centrifuged so that the lipid components were separated to enable the NMR of creatine.

NE activates 5' AMP-activated protein kinase phosphorylation through the β_3 -adrenoreceptor to increase the glucose uptake of BAT^{59,60}. BAT thermogenesis is activated after NE stimulation by the consumption of fatty acids and glucose⁶¹. Triglyceride breakdown provides fuel to support thermogenesis, regulated by UCP1 and UCP1-independent thermogenic mechanisms such as the futile creatine cycle⁶². However, our experiments in rats found that the effect due to 1.0 mg kg⁻¹ of NE was not detectable with $[^{18}\text{F}]$ FDG PET as significant ($P > 0.05$) until the NE dosage was increased to 2.5 mg kg⁻¹, which is consistent with previous studies^{63,64}.

When mammals are exposed to cold, sympathetic nerves release NE, which activates brown adipocytes and induces thermogenesis⁶⁵. In our experiments involving cold-stimulated rats and humans, BAT showed increased Cr-CEST contrast. Our *in vivo* human experiments

before and after cold exposure also demonstrated the feasibility of the proposed Cr-CEST method to assess BAT activation in the context of clinical 3T applications. Many factors (for example, age, BMI) affect BAT activation⁶⁶. The variation in baseline Cr-CEST in healthy adults in our study was significantly correlated to BMI, which is consistent with previous reports^{66–68}.

In addition to BAT, beige adipocytes exhibit thermogenesis via the futile creatine cycle^{18,19}. However, studying beige fat activation with the Cr-CEST we developed in this study requires higher detection sensitivity and spatial resolution, which will be the focus of our future work.

FDG PET imaging is based on the uptake of exogenous FDG, providing a readout of activated BAT. In contrast, a major advantage to using Cr-CEST is that as it provides endogenous imaging of tissue creatine, it allows BAT detection at rest and during activation. Therefore, unlike FDG PET, all volunteers showed positive Cr-CEST signals in BAT at baseline and after activation.

Of note, 50 volunteers were recruited for MRI to study baseline Cr-CEST variations dependent on BMI. Among these 50 healthy volunteers, 14 were randomly selected for PET and CT imaging. It is a limitation of this study that uneven numbers of individuals were recruited for MRI and PET. Thus, only a moderate correlation was found between Cr-CEST MRI and [¹⁸F]FDG PET. These data cannot be used to compare the detection sensitivity or statistical power between MRI and PET.

Currently, Dixon imaging and T2* mapping are the most commonly used MRI methods to differentiate BAT from WAT. Dixon imaging has an established track record for fat imaging and can differentiate BAT from WAT based on FWF^{27,69}. T2* mapping has been exploited to differentiate between WAT and BAT based on the presence of iron in the mitochondria of BAT⁷⁰. Because of the short imaging time, both methods usually have a high temporal and spatial resolution, making them incomparable for both acute monitoring and volumetric measurement of three-dimensional (3D) imaging⁷¹. However, both Dixon imaging and T2* mapping methods suffer from the ever-present sensitivity to phase wrapping and the inhomogeneities of the static B₀ field⁷². More importantly, Dixon imaging provides mainly BAT mass-based information that is insensitive to adipocyte metabolic function⁷³. The Cr-CEST contrast fitted from the whole Z-spectrum is inherently insensitive to phase wrapping and field inhomogeneity compared with Dixon imaging and T2* mapping. CEST Z-spectrum MRI can simultaneously obtain the FWF⁷⁴ and creatine-mediated BAT function through Z-spectral fitting, realizing the combination of fat content and adipocyte metabolic function imaging.

The inevitable partial volume contamination of BAT by WAT and other ‘fat’ components (‘browning WAT’ and ‘beige adipocytes’) is a common challenge for MRI and PET imaging. However, the metabolic activity of adipose tissues measured with Cr-CEST (%) is a physiological parameter that is independent of tissue composition. Higher Cr-CEST means higher metabolic activity across all adipose tissue types in a general sequence of BAT > beige adipocytes > browning WAT > WAT. We further demonstrated that by increasing the spatial resolution of Cr-CEST, the partial volume effect can be reduced and the tissue boundaries are clearer. Furthermore, we also tried multi-slice Cr-CEST imaging in the rat interscapular BAT; the Cr-CEST signal of the whole BAT increased significantly after pharmacological stimulation.

As a limitation, the acquisition time for Cr-CEST imaging based on the full Z-spectral acquisition may prevent the capture of rapid creatine changes because of acute BAT activation. Recent studies demonstrated rapid 3D acquisition of CEST imaging by using multi-tasking⁷⁵, multi-slice⁷⁶ and snapshot⁷⁷ acquisition. Hence, it may be feasible to capture rapid changes in creatine signals and 3D volumetric measurements of metabolically active BAT by incorporating these fast imaging sequences.

The duration and severity of obesity are positively associated with incident metabolic syndrome^{78–80}, including T2D and cardiometabolic

diseases. Early detection of the severity and complications of metabolic syndrome through metabolic or functional imaging of adipose tissues will be useful to prescribe effective interventions and lifestyle changes^{81–84}. MRI offers the advantage of no radiation exposure compared to PET and CT and has gained popularity in the management of clinical obesity, especially for patients with T2D who cannot undergo [¹⁸F]FDG PET and CT imaging^{85,86}. We demonstrated the feasibility of the endogenous metabolic Cr-CEST MRI technique in mapping BAT activity in rodents and humans. Endogenous Cr-CEST MRI may provide molecular insight into the pathogenesis, help with early detection and risk stratification, and serve as a biomarker for developing, evaluating and guiding new treatment strategies for metabolic diseases, using longitudinal and noninvasive means. Treatment evaluation and monitoring with the advanced Cr-CEST MRI may greatly enhance treatment efficacy and therefore reduce the socio-economic costs due to obesity.

Methods

Animal experiments

All animal experiments were approved by the Institutional Animal Use and Care Committee of Guangdong Provincial People’s Hospital. Sprague Dawley rats (male, 8 weeks old, 250–300 g) were obtained from Guangdong Medical Laboratory Animal Center. Rats were housed at 23 °C with free access to water and food under a 12/12 h light–dark cycle.

In vivo 7T rat MRI

The rat MRI experiments were performed using a 7T small-bore MRI scanner (Bruker Biospec). Briefly, after fasted overnight, rats were anaesthetized (induced by 3.0% isoflurane, maintained with 1.5–2.0% isoflurane) and scanned in a supine position. A water-heated pad was used to maintain the body temperature of rats at 37 °C, and a balloon pressure sensor was placed on the abdomen for respiratory gating. Continuous physiological monitoring (rectal temperature, respiratory rate) was performed throughout the experiments using an MRI-compatible small-animal monitoring system (Small Animal Instruments).

Cr-CEST MRI was used to dynamically image interscapular fat every 10 min for up to 2 h after intraperitoneal injection of saline, NE or β_3 -adrenergic receptor agonists (CL, 1.0 mg kg⁻¹ or 2.5 mg kg⁻¹ body weight, Sigma-Aldrich). For the cold exposure experiment, rats were singly placed in individual precooled cages without bedding at 4 °C for 2 h in climate-controlled cold rooms. Cr-CEST MRI was performed on rats at room temperature and under cold exposure.

Cr-CEST Z-spectra were acquired from the central slice of the interscapular fat depot in rats with a pre-saturation pulse of 1 μ T for 3 s (unless specified otherwise), followed by a rapid acquisition with relaxation enhancement (RARE) readout. Each Z-spectrum contained 54 images at varied frequency offsets, from -6 to 6 ppm at step-sizes of 0.25, ±8, ±10; +300 ppm was used as the reference image. The other imaging parameters were echo time (TE) = 3.6 ms; repetition time (TR) = 8,000 ms; field of view (FOV) = 40 × 40 mm²; matrix size = 100 × 100; in-plane resolution = 0.4 × 0.4 mm²; slice thickness = 1.5 mm; number of averages = 1; RARE factor = 36; and total acquisition time = 7 min 12 s.

To investigate the influence of spatial resolution, high-resolution Cr-CEST images were acquired similarly except for matrix size = 256 × 256; in-plane resolution = 0.156 × 0.156 mm²; number of averages = 2; TE = 4 ms; TR = 5,000 ms; 24 offsets (±10, ±7.5, ±5, ±4, ±3.5, ±3, ±2, ±1, ±0.5, 0, +2.5, +2.25, +1.75, +1.5 and +300 ppm); and acquisition time = 16 min. Low-resolution Cr-CEST was acquired with a matrix size = 128 × 128; in-plane resolution = 0.31 × 0.31 mm²; number of averages = 2; and acquisition time = 8 min. Multi-slice Z-spectra were acquired from three rats similarly, with 11 slices covering the entire interscapular BAT with TR = 3.2 s and a total acquisition time of 14 min.

All image processing and data analysis was performed in MATLAB (v.R2020a, MathWorks). Raw Z-spectral images (M_z) were normalized with the reference image at +300 ppm (M_0), carefully corrected for B_0 inhomogeneities on a pixel-by-pixel basis in reference to water (0 ppm) or fat (-3.4 ppm) signal in fat-dominant tissues (the process of Z-spectral fitting further fine-tunes the water or fat resonances), reversed to $1-M_z/M_0$ and then fitted to multi-Lorentzian functions containing the direct saturation of water and the main methylene fat, Cr-CEST, APT and broadband MT spectrum according to equations (1) and (2):

$$Z(\omega) = \sum_{i=1}^n L_i(\omega) \quad (1)$$

$$L_i(\omega) = \frac{A}{1 + 4\left(\frac{\omega - \omega_0}{l\omega}\right)^2} \quad (2)$$

where A , ω_0 and $l\omega$ are the amplitude, centre frequency offset and line width of each peak, respectively.

The values and parameters for the first and second rounds of fittings are listed in Table 1. Three dominant components, including the direct saturation of bulk water, the main methylene fat and the MT peaks, were subtracted from the raw Z-spectrum and underwent a secondary fitting for the remaining two small peaks of Cr-CEST and APT. Motion artefacts during the 2 h Cr-CEST data acquisition were corrected by MATLAB's intensity-based image registration routine imregister. Cr-CEST signals were averaged within the regions of interest (ROIs) of the central area of the interscapular BAT and WAT in reference to the corresponding T2-weighted images.

In vivo [¹⁸F]FDG PET and CT rat imaging

The rat [¹⁸F]FDG PET and CT experiments were performed using a Micro-PET/CT system (IRIS PET/CT, Inviscan). Briefly, after fasting for 8 h (required for PET studies), each rat was anaesthetized (induced by 3.0% isoflurane and maintained with 1.5–2.0% isoflurane) and placed onto the imaging bed in a supine position. A heated constant temperature airflow was used to maintain body temperature at 37 °C, and a balloon pressure sensor was placed on the abdomen for respiratory gating. Continuous physiological monitoring (rectal temperature, respiratory rate) was performed throughout the experiments using a small-animal monitoring system (Équipement Vétérinaire MINERVE).

Saline, NE (1.0 mg kg⁻¹ and 2.5 mg kg⁻¹), and CL (1.0 mg kg⁻¹) were administered via intraperitoneal injection; at the same time, an intravenous injection of [¹⁸F]FDG (approximately 500 µCi) was administered via the rat's lateral tail vein. Dynamic PET data were acquired to detect the glucose uptake of BAT for up to 2 h after an injection of either saline, NE or CL. After the PET scan, CT acquisition was performed at 80 kV and 0.9 mA, with a total acquisition time of 20 s. For PET quantification, the SUV_{mean} of interscapular BAT and WAT was measured in manually drawn ROIs in reference to the CT anatomical images.

Human studies

The protocol for the human studies was approved by the Institutional Review Board of Guangdong Provincial People's Hospital (no. KY-Q-2022-102-06). All participants provided written informed consent before the experiment. Fifty young and healthy volunteers (27 male, 23 female; age = 22.42 ± 1.85, BMI = 21.31 ± 3.51, mean ± s.d.) were recruited for Cr-CEST imaging of BAT activation at room temperature and 120 min after cold exposure. [¹⁸F]FDG PET and CT imaging was performed with a Biograph mCT Flow 64 PET/CT system (Siemens Healthcare) on 14 of the participants at room temperature and after 120 min of mild cold exposure.

Before each MRI or PET and CT imaging session, individuals were required to refrain from alcohol, caffeine, medication and exercise for

the previous 48 h and to fast overnight (>8 h). The study flowchart is shown in Fig. 5. Briefly, on the first day, Cr-CEST imaging was performed in a 3T whole-body MRI scanner (Ingenia CX, Philips Healthcare) with a 32-channel surface receiving coil on the volunteers' interscapular BAT region at room temperature (25 °C). Then, volunteers were transferred to an room temperature of 16–17 °C and wore a 6–10 °C cooling vest with ice packs for 120 min (changed every 30 min) to collect the cold-exposed Cr-CEST data.

For Cr-CEST imaging, the parameters of the turbo spin-echo-CEST sequence remained the same as in the in vivo rat experiments except for TE = 6.9 ms; TR = 6,000 ms; FOV = 500 × 500 mm²; reconstructed matrix size = 512 × 512; slice thickness = 5 mm; echo train length = 156; and total acquisition time = 5 min 30 s. The Cr-CEST post-processing procedure in the human studies was consistent with that in the rat studies. BAT and WAT Cr-CEST signals were quantified by drawing the ROI on the central area of the interscapular and subcutaneous abdominal, respectively, using T2-weighted images as anatomical references.

The PET and CT studies of 14 participants (age = 22.00 ± 1.47; sex = 7 male and 7 female; BMI = 20.67 ± 2.05, mean ± s.d.) were performed 2 weeks after the MRI. CT scans were performed at 120 kV, 230 mAs and 3-mm thickness of layers, followed by a PET scan. For the PET and CT studies at RT, 5 mCi [¹⁸F]FDG was injected intravenously into each participant. The PET and CT scans were acquired 60 min later. Two weeks later, volunteers were invited back for a second PET and CT scan after being exposed to the cold and wore a 6–10 °C cooling vest with ice packs for 60 min (changed every 30 min). During cold exposure, individuals wore shorts and T-shirts for sedentary activities, such as reading a book and watching TV, and were instructed to avoid physical activity. 5 mCi of [¹⁸F]FDG was injected intravenously into each volunteer. After another 60 min of cold exposure with the cooling vest on, a PET and CT was performed. The SUV_{mean} of the central area of the interscapular BAT and subcutaneous abdominal WAT was measured in manually drawn ROIs according to the BARCIST standard²³ in reference to the CT anatomical images (Hounsfield units were between -190 and -10, avoiding the glands, blood vessels, skeletal muscles and air spaces). Two different operators (both with more than 3 years of experience in BAT imaging research) delineated the ROI separately and showed a good interclass correlation coefficient of 0.90 ($P < 0.0001$).

Phantom preparation and MRI

Phantoms ($n = 3$ sets) contained vials with creatine concentrations of 2.5 mM, 5.0 mM, 7.5 mM, 10 mM, 15 mM, and 20 mM in PBS (pH 7.0). The temperature of the phantom was controlled with a hot-water pad and monitored with a temperature probe; the corresponding Cr-CEST MRI data were collected at 35 °C, 37 °C and 39 °C. Cr-CEST Z-spectra were acquired from the central slice of the phantom with a pre-saturation pulse of 1 µT for 3 s, followed by a RARE readout. Each Z-spectrum contained 54 images at varied frequency offsets containing from -6 to 6 ppm at step-sizes of 0.25 ppm, ±8, ±10, with +300 ppm used as the reference image. The other imaging parameters were TE = 3.6 ms; TR = 6,000 ms; FOV = 40 × 40 mm²; matrix size = 160 × 160; in-plane resolution = 0.25 × 0.25 mm²; slice thickness = 1.0 mm; number of averages = 1; RARE factor = 89; and total acquisition time = 5 min 24 s.

B_0 field maps

For Z-spectral fitting-based B_0 mapping, B_0 inhomogeneities from the Cr-CEST data were corrected with reference to the water (0 ppm) or fat (-3.4 ppm) signal in fat-dominant tissues. The process of Z-spectral fitting further fine-tunes the water or fat resonance.

For WASSR-based B_0 mapping, the B_0 field map was defined as the offset of the water peak in the Z-spectra with reference to 0 ppm. WASSR data from rats were acquired with a pre-saturation pulse of 0.5 µT for 500 ms followed by a RARE readout. Each Z-spectrum contained 42 images at varied frequency offsets containing from -2 to 2 ppm at step-sizes of 0.1 ppm; +300 ppm was used as the

reference image. The other imaging parameters were TE = 3.6 ms; TR = 1,500 ms; FOV = 40 × 40 mm²; matrix size = 160 × 160; in-plane resolution = 0.25 × 0.25 mm²; slice thickness = 1.5 mm; number of averages = 1; RARE factor = 89; and total acquisition time = 1 min 3 s.

B₁ field maps

B₁ field maps from rats were obtained using a two-dimensional single-slice RARE readout sequence with TE = 10 ms; TR = 10,000 ms; FOV = 40 × 40 mm²; and matrix size = 80 × 80. Two images were obtained using preparation pulses with 60° and 120° flip angles. The actual flip angle (θ) for each pixel was calculated as shown in equation (3).

$$\frac{\cos(2\theta)}{\cos(\theta)} = \frac{I(120^\circ)}{I(60^\circ)} \quad (3)$$

where I(60°) and I(120°) denote pixel signals with 60° and 120° preparation flip angles, respectively. The relative B₁ map was constructed as 9/60° for each pixel.

B₁ field maps from humans were obtained similarly except for TE = 50 ms; TR = 6,000 ms; FOV = 500 × 500 mm²; and matrix size = 400 × 400.

Gene expression analysis (quantitative PCR with reverse transcription)

Total RNA was extracted from frozen tissue using the TRNzol Universal Reagent (TIANGEN Biotech) and quantified using a NanoDrop 2000 ultraviolet-visible spectrophotometer (Thermo Fisher Scientific). Using quantitative PCR with reverse transcription (RT-qPCR) and the PrimeScript RT Reagent Kit (Takara Bio), complementary DNA (cDNA) was prepared using 1 µg total RNA. RT-qPCR was performed on cDNA using the TB Green Premix EX Taq II kit (Takara Bio) and the CFX96 Real-Time PCR Detection System (Bio-Rad Laboratories). Normalized mRNA expression was calculated with the 2^{-ΔΔCt} method, using vinculin (VCL) mRNA as the reference. Primer sequences used for the RT-qPCR of the rat samples are as follows: *Pparg1α* (forward ACACATCG CAATTCTCCCTTGTA; reverse CTTTCAGACTCCCGCTTCTCATA); *Ckb* (forward AAGACTGACCTCAACCCAGACAA; reverse CTTCTA CTGCCAG CTTCTCGATG); *Dio2* (forward GCCAACGTAGCTTATGGGGT; reverse TTCTCCAGC CAACTTCGGAC); *Ucp1* (forward TCTACGATACGGTCCAA GAGTACT; reverse AAGCATTGTAGGTCCCAGTGTAG); *Vcl* (forward CTGACCTCCTGCTTACCTTTGAT; reverse GCAGCTTTGACA GTGTTCAATT).

¹H-NMR spectroscopy

Brown fat tissue samples (approximately 200 mg) were freeze-dried for at least 36 h in a SpeedVac. Dehydrated tissue was homogenized in PBS buffer, pH 7.4, and centrifuged at 13,000g for 10 min at 4 °C; the soluble liquid below the fat cake was transferred to a new tube after centrifugation. The supernatant was reconstituted in a 600 µl mixture containing 550 µl PBS buffer and 50 µl tetramethylsilane (TMS) in D₂O (99.9% D₂O + 0.05% TMS v/v), vortex-mixed for 60 s and transferred to 5-mm NMR tubes. The ¹H-NMR spectra were acquired with a Bruker 600 MHz Avance III HD spectrometer (Bruker Biospec). ¹H-NMR spectra were recorded using a one-dimensional CPMG pulse sequence; the acquisition parameters were: number of scans 64; 90° pulse width, 11.4 µs; acquisition time 2.73 s; and relaxation delay 4.0 s. The spectrum was then phase-adjusted manually, followed by baseline correction and frequency alignment with reference to the 0 ppm TMS signal using MestReNova v.14.0 (Mestrelab Research). Metabolites were identified and quantified by fitting the spectral lines of the library compounds into the recorded ¹H-NMR spectrum of the tissue extract. Absolute quantification was based on the peak amplitude of the TMS signal. Metabolite concentrations are exported as mmol l⁻¹ in the NMR sample.

Metabolic cages

Rats were fasted overnight and single-housed in metabolic chambers (Promethion high-definition behavioural phenotyping system, Sable Systems International) for respiratory monitoring. After measuring the basic metabolic rate for 30 min without interruption. Rats were injected intraperitoneally with saline, NE or CL at the dose of 1.0 mg kg⁻¹ body weight; oxygen consumption (VO₂) was recorded every 3 min for 2 h using the Sable Systems data acquisition software. Data were parsed and analysed using the Sable Systems International Macro Interpreter software (v.22.10) using the One Click Macro (v.2.51.4).

Statistical analysis

Sample numbers, the number of biological replicates and the statistical analysis methods used are provided in the figure legends. Statistical analysis was performed using Prism v.8.3.0 (GraphPad Software). All statistical tests are fully described in the figure legends and meet the criteria for a normal distribution with similar variance. Two-tailed Student's *t*-tests were used for comparisons between two groups. Data are presented as the mean ± s.e.m. unless otherwise stated. *P*<0.05 was deemed statistically significant.

Reporting summary

Further information on research design is available in the Nature Portfolio Reporting Summary linked to this article.

Data availability

All source data are provided as Supplementary Information. Source data are provided with this paper.

References

- Blüher, M. Obesity: global epidemiology and pathogenesis. *Nat. Rev. Endocrinol.* **15**, 288–298 (2019).
- Piché, M. E., Tchernof, A. & Després, J. P. Obesity phenotypes, diabetes, and cardiovascular diseases. *Circ. Res.* **126**, 1477–1500 (2020).
- Deng, T., Lyon, C. J., Bergin, S., Caligiuri, M. A. & Hsueh, W. A. Obesity, inflammation, and cancer. *Annu. Rev. Pathol.* **11**, 421–449 (2016).
- Kahn, B. B. & Flier, J. S. Obesity and insulin resistance. *J. Clin. Invest.* **106**, 473–481 (2000).
- Müller, T. D., Blüher, M., Tschoep, M. H. & DiMarchi, R. D. Anti-obesity drug discovery: advances and challenges. *Nat. Rev. Drug Discov.* **21**, 201–223 (2022).
- Dixon, J. B., Straznicky, N. E., Lambert, E. A., Schlaich, M. P. & Lambert, G. W. Surgical approaches to the treatment of obesity. *Nat. Rev. Gastroenterol. Hepatol.* **8**, 429–437 (2011).
- Wu, J. et al. Beige adipocytes are a distinct type of thermogenic fat cell in mouse and human. *Cell* **150**, 366–376 (2012).
- Ruiz, J. R. et al. Role of human brown fat in obesity, metabolism and cardiovascular disease: strategies to turn up the heat. *Prog. Cardiovasc. Dis.* **61**, 232–245 (2018).
- Roman, S. et al. Brown adipose tissue and novel therapeutic approaches to treat metabolic disorders. *Transl. Res.* **165**, 464–479 (2015).
- Liew, C. W. et al. Ablation of *TRIP-Br2*, a regulator of fat lipolysis, thermogenesis and oxidative metabolism, prevents diet-induced obesity and insulin resistance. *Nat. Med.* **19**, 217–226 (2013).
- Moisan, A. et al. White-to-brown metabolic conversion of human adipocytes by JAK inhibition. *Nat. Cell Biol.* **17**, 57–67 (2015).
- Rosenwald, M., Perdikari, A., Rulicke, T. & Wolfrum, C. Bi-directional interconversion of brite and white adipocytes. *Nat. Cell Biol.* **15**, 659–667 (2013).
- Chouchani, E. T., Kazak, L. & Spiegelman, B. M. New advances in adaptive thermogenesis: UCP1 and beyond. *Cell Metab.* **29**, 27–37 (2019).

14. Guan, H.-P. et al. A futile metabolic cycle activated in adipocytes by antidiabetic agents. *Nat. Med.* **8**, 1122–1128 (2002).
15. Reshef, L. et al. Glyceroneogenesis and the triglyceride/fatty acid cycle. *J. Biol. Chem.* **278**, 30413–30416 (2003).
16. Prentki, M. & Madiraju, S. R. M. Glycerolipid metabolism and signaling in health and disease. *Endocrine Rev.* **29**, 647–676 (2008).
17. Wunderling, K., Zurkovic, J., Zink, F., Kuerschner, L. & Thiele, C. Triglyceride cycling enables modification of stored fatty acids. *Nat. Metab.* **5**, 699–709 (2023).
18. Kazak, L. et al. A creatine-driven substrate cycle enhances energy expenditure and thermogenesis in beige fat. *Cell* **163**, 643–655 (2015).
19. Bertholet, A. M. et al. Mitochondrial patch clamp of beige adipocytes reveals UCP1-positive and UCP1-negative cells both exhibiting futile creatine cycling. *Cell Metab.* **25**, 811–822 (2017).
20. Rahbani, J. F. et al. Creatine kinase B controls futile creatine cycling in thermogenic fat. *Nature* **590**, 480–485 (2021).
21. Rahbani, J. F. et al. Parallel control of cold-triggered adipocyte thermogenesis by UCP1 and CKB. *Cell Metab.* **36**, 526–540 (2024).
22. Ikeda, K. et al. UCP1-independent signaling involving SERCA2b-mediated calcium cycling regulates beige fat thermogenesis and systemic glucose homeostasis. *Nat. Med.* **23**, 1454–1465 (2017).
23. Chen, K. Y. et al. Brown Adipose Reporting Criteria in Imaging STudies (BARCIST 1.0): recommendations for standardized FDG-PET/CT experiments in humans. *Cell Metab.* **24**, 210–222 (2016).
24. Cypess, A. M. et al. Identification and importance of brown adipose tissue in adult humans. *N. Engl. J. Med.* **360**, 1509–1517 (2009).
25. Hamilton, G., Smith, D. L. Jr., Bydder, M., Nayak, K. S. & Hu, H. H. MR properties of brown and white adipose tissues. *J. Magn. Reson. Imaging* **34**, 468–473 (2011).
26. Hankir, M. K. & Klingenspor, M. Brown adipocyte glucose metabolism: a heated subject. *EMBO Rep.* **19**, e46404 (2018).
27. Chen, Y. C. et al. Measurement of human brown adipose tissue volume and activity using anatomic MR imaging and functional MR imaging. *J. Nucl. Med.* **54**, 1584–1587 (2013).
28. Wu, B. et al. An overview of CEST MRI for non-MR physicists. *EJNMMI Phys.* **3**, 19 (2016).
29. Khlebnikov, V., van der Kemp, W. J. M., Hoogduin, H., Klomp, D. W. J. & Prompers, J. J. Analysis of chemical exchange saturation transfer contributions from brain metabolites to the Z-spectra at various field strengths and pH. *Sci. Rep.* **9**, 1089 (2019).
30. Zhou, J. et al. Differentiation between glioma and radiation necrosis using molecular magnetic resonance imaging of endogenous proteins and peptides. *Nat. Med.* **17**, 130–134 (2011).
31. van Zijl, P. C. M., Jones, C. K., Ren, J., Malloy, C. R. & Sherry, A. D. MRI detection of glycogen in vivo by using chemical exchange saturation transfer imaging (glycoCEST). *Proc. Natl Acad. Sci. USA* **104**, 4359–4364 (2007).
32. Ling, W., Regatte, R. R., Navon, G. & Jerschow, A. Assessment of glycosaminoglycan concentration in vivo by chemical exchange-dependent saturation transfer (gagCEST). *Proc. Natl Acad. Sci. USA* **105**, 2266–2270 (2008).
33. Cai, K. et al. Magnetic resonance imaging of glutamate. *Nat. Med.* **18**, 302–306 (2012).
34. Singh, A. et al. Evaluating the feasibility of creatine-weighted CEST MRI in human brain at 7T using a Z-spectral fitting approach. *NMR Biomed.* **32**, e4176 (2019).
35. Cai, K. et al. CEST signal at 2ppm (CEST@2ppm) from Z-spectral fitting correlates with creatine distribution in brain tumor. *NMR Biomed.* **28**, 1–8 (2015).
36. Cai, K. et al. Creatine CEST MRI for differentiating gliomas with different degrees of aggressiveness. *Mol. Imaging Biol.* **19**, 225–232 (2017).
37. Haris, M. et al. A technique for in vivo mapping of myocardial creatine kinase metabolism. *Nat. Med.* **20**, 209–214 (2014).
38. Kogan, F. et al. Method for high-resolution imaging of creatine in vivo using chemical exchange saturation transfer. *Magn. Reson. Med.* **71**, 164–172 (2014).
39. Kogan, F. et al. In vivo chemical exchange saturation transfer imaging of creatine (CrCEST) in skeletal muscle at 3T. *J. Magn. Reson. Imaging* **40**, 596–602 (2014).
40. Berlet, H. H., Bonsmann, I. & Birringer, H. Occurrence of free creatine, phosphocreatine and creatine phosphokinase in adipose tissue. *Biochim. Biophys. Acta* **437**, 166–174 (1976).
41. Sun, P. Z., Zhou, J., Sun, W., Huang, J. & van Zijl, P. C. Suppression of lipid artifacts in amide proton transfer imaging. *Magn. Reson. Med.* **54**, 222–225 (2005).
42. Dula, A. N. et al. Amide proton transfer imaging of the breast at 3 T: establishing reproducibility and possible feasibility assessing chemotherapy response. *Magn. Reson. Med.* **70**, 216–224 (2013).
43. Zhang, X.-Y. et al. Assignment of the molecular origins of CEST signals at 2 ppm in rat brain. *Magn. Reson. Med.* **78**, 881–887 (2017).
44. Zhou, J., Lal, B., Wilson, D. A., Laterra, J. & van Zijl, P. C. Amide proton transfer (APT) contrast for imaging of brain tumors. *Magn. Reson. Med.* **50**, 1120–1126 (2003).
45. Zhou, J. Amide proton transfer imaging of the human brain. *Methods Mol. Biol.* **711**, 227–237 (2011).
46. Berbée, J. F. et al. Brown fat activation reduces hypercholesterolaemia and protects from atherosclerosis development. *Nat. Commun.* **6**, 6356 (2015).
47. Murala, S. & Bollu, P. C. Norepinephrine. In *Neurochemistry in Clinical Practice* (ed. Bollu, P. C.) 165–179 (Springer, 2022).
48. Atgié, C., D'Allaire, F. & Bukowiecki, L. J. Role of beta1- and beta3-adrenoceptors in the regulation of lipolysis and thermogenesis in rat brown adipocytes. *Am. J. Physiol.* **273**, C1136–C1142 (1997).
49. van der Lans, A. A. et al. Cold acclimation recruits human brown fat and increases nonshivering thermogenesis. *J. Clin. Invest.* **123**, 3395–3403 (2013).
50. Søberg, S. et al. Altered brown fat thermoregulation and enhanced cold-induced thermogenesis in young, healthy, winter-swimming men. *Cell Rep. Med.* **2**, 100408 (2021).
51. van Marken Lichtenbelt, W. D. et al. Cold-activated brown adipose tissue in healthy men. *N. Engl. J. Med.* **360**, 1500–1508 (2009).
52. Law, J. et al. Thermal imaging is a noninvasive alternative to PET/CT for measurement of brown adipose tissue activity in humans. *J. Nucl. Med.* **59**, 516–522 (2018).
53. Sun, Y. et al. Mitochondrial TNAP controls thermogenesis by hydrolysis of phosphocreatine. *Nature* **593**, 580–585 (2021).
54. Haris, M. et al. Exchange rates of creatine kinase metabolites: feasibility of imaging creatine by chemical exchange saturation transfer MRI. *NMR Biomed.* **25**, 1305–1309 (2012).
55. Chen, L., Barker, P. B., Weiss, R. G., van Zijl, P. C. M. & Xu, J. Creatine and phosphocreatine mapping of mouse skeletal muscle by a polynomial and Lorentzian line-shape fitting CEST method. *Magn. Reson. Med.* **81**, 69–78 (2019).
56. Chen, L. et al. Investigation of the contribution of total creatine to the CEST Z-spectrum of brain using a knockout mouse model. *NMR Biomed.* **30**, e3834 (2017).
57. Pavuluri, K., Rosenberg, J. T., Helsper, S., Bo, S. & McMahon, M. T. Amplified detection of phosphocreatine and creatine after supplementation using CEST MRI at high and ultrahigh magnetic fields. *J. Magn. Reson.* **313**, 106703 (2020).

58. Chung, J. J., Jin, T., Lee, J. H. & Kim, S.-G. Chemical exchange saturation transfer imaging of phosphocreatine in the muscle. *Magn. Reson. Med.* **81**, 3476–3487 (2019).
59. Hutchinson, D. S., Chernogubova, E., Dallner, O. S., Cannon, B. & Bengtsson, T. Beta-adrenoceptors, but not alpha-adrenoceptors, stimulate AMP-activated protein kinase in brown adipocytes independently of uncoupling protein-1. *Diabetologia* **48**, 2386–2395 (2005).
60. Chernogubova, E., Cannon, B. & Bengtsson, T. Norepinephrine increases glucose transport in brown adipocytes via beta3-adrenoceptors through a cAMP, PKA, and PI3-kinase-dependent pathway stimulating conventional and novel PKCs. *Endocrinology* **145**, 269–280 (2004).
61. Inokuma, K. et al. Uncoupling protein 1 is necessary for norepinephrine-induced glucose utilization in brown adipose tissue. *Diabetes* **54**, 1385–1391 (2005).
62. Roesler, A. & Kazak, L. UCP1-independent thermogenesis. *Biochem. J.* **477**, 709–725 (2020).
63. Carey, A. L. et al. Ephedrine activates brown adipose tissue in lean but not obese humans. *Diabetologia* **56**, 147–155 (2013).
64. Cypess, A. M. et al. Cold but not sympathomimetics activates human brown adipose tissue in vivo. *Proc. Natl Acad. Sci. USA* **109**, 10001–10005 (2012).
65. Li, L., Li, B., Li, M. & Speakman, J. R. Switching on the furnace: regulation of heat production in brown adipose tissue. *Mol. Aspects Med.* **68**, 60–73 (2019).
66. Steinberg, J. D., Vogel, W. & Vegt, E. Factors influencing brown fat activation in FDG PET/CT: a retrospective analysis of 15,000+ cases. *Br. J. Radiol.* **90**, 20170093 (2017).
67. Wang, Q. et al. Brown adipose tissue activation is inversely related to central obesity and metabolic parameters in adult human. *PLoS ONE* **10**, e0123795 (2015).
68. Becher, T. et al. Brown adipose tissue is associated with cardiometabolic health. *Nat. Med.* **27**, 58–65 (2021).
69. Cypess, A. M., Haft, C. R., Laughlin, M. R. & Hu, H. H. Brown fat in humans: consensus points and experimental guidelines. *Cell Metab.* **20**, 408–415 (2014).
70. Holstila, M. et al. MR signal-fat-fraction analysis and T2* weighted imaging measure BAT reliably on humans without cold exposure. *Metabolism* **70**, 23–30 (2017).
71. Henninger, B. et al. Performance of different Dixon-based methods for MR liver iron assessment in comparison to a biopsy-validated R2* relaxometry method. *Eur. Radiol.* **31**, 2252–2262 (2021).
72. Ladefoged, C. N. et al. Impact of incorrect tissue classification in Dixon-based MR-AC: fat-water tissue inversion. *EJNMMI Phys.* **1**, 101 (2014).
73. Ma, J. Dixon techniques for water and fat imaging. *J. Magn. Reson. Imaging* **28**, 543–558 (2008).
74. Scotti, A. et al. Mapping brown adipose tissue based on fat water fraction provided by Z-spectral imaging. *J. Magn. Reson. Imaging* **47**, 1527–1533 (2018).
75. Han, P. et al. Whole-brain steady-state CEST at 3 T using MR multitasking. *Magn. Reson. Med.* **87**, 2363–2371 (2022).
76. Villano, D. et al. A fast multislice sequence for 3D MRI-CEST pH imaging. *Magn. Reson. Med.* **85**, 1335–1349 (2021).
77. Akbey, S., Ehses, P., Stirnberg, R., Zaiss, M. & Stöcker, T. Whole-brain snapshot CEST imaging at 7 T using 3D-EPI. *Magn. Reson. Med.* **82**, 1741–1752 (2019).
78. Mongraw-Chaffin, M. et al. Obesity severity and duration are associated with incident metabolic syndrome: evidence against metabolically healthy obesity from the multi-ethnic study of atherosclerosis. *J. Clin. Endocrinol. Metab.* **101**, 4117–4124 (2016).
79. Nguyen, N. T., Magno, C. P., Lane, K. T., Hinojosa, M. W. & Lane, J. S. Association of hypertension, diabetes, dyslipidemia, and metabolic syndrome with obesity: findings from the National Health and Nutrition Examination Survey, 1999 to 2004. *J. Am. Coll. Surg.* **207**, 928–934 (2008).
80. McKenney, R. L. & Short, D. K. Tipping the balance: the pathophysiology of obesity and type 2 diabetes mellitus. *Surg. Clin. North Am.* **91**, 1139–1148 (2011).
81. Kee, C. C. et al. Association of BMI with risk of CVD mortality and all-cause mortality. *Public Health Nutr.* **20**, 1226–1234 (2017).
82. Flegal, K. M., Kit, B. K., Orpana, H. & Graubard, B. I. Association of all-cause mortality with overweight and obesity using standard body mass index categories: a systematic review and meta-analysis. *JAMA* **309**, 71–82 (2013).
83. Selwyn, A. P. Weight reduction and cardiovascular and metabolic disease prevention: clinical trial update. *Am. J. Cardiol.* **100**, 33P–37P (2007).
84. Cohen, J. B. & Cohen, D. L. Cardiovascular and renal effects of weight reduction in obesity and the metabolic syndrome. *Curr. Hypertens. Rep.* **17**, 34 (2015).
85. Kim, S. R. & Lerman, L. O. Diagnostic imaging in the management of patients with metabolic syndrome. *Transl. Res.* **194**, 1–18 (2018).
86. Mitra, S., Fernandez-Del-Valle, M. & Hill, J. E. The role of MRI in understanding the underlying mechanisms in obesity associated diseases. *Biochim. Biophys. Acta Mol. Basis Dis.* **1863**, 1115–1131 (2017).

Acknowledgements

We thank Z. Zhuoli from the University of California, Irvine for his helpful discussion. We also thank Z. Wenzhen and L. Li from Tongji Hospital, and S. Alessandro from GE Healthcare. This work is supported by the National Science Fund for Distinguished Young Scholars of China (no. 81925023 to Z.L.); the Regional Innovation and Development Joint Fund of the National Natural Science Foundation of China (no. U22A20345 to Z.L.); the National Key R&D Program of China (no. 2021YFF1201003 to Z.L.); the Key-Area Research and Development Program of Guangdong Province, China (no. 2021B0101420006 to Z.L.; nos. 2018B030340001 and 2018B030333001 to Y.F.); the Guangdong Provincial Key Laboratory of Artificial Intelligence in Medical Image Analysis and Application (no. 2022B1212010011 to Z.L.); the High-level Hospital Construction Project (no. DFJHBF202105 to Z.L.); and the National Natural Science Foundation of China (no. U21A6005 to Y.F.). The research reported in this article was also supported by the National Institutes of Health (NIH) under award nos. R01DK135722 and R01CA283548 to K.C. The content is solely the responsibility of the authors and does not necessarily represent the official views of the NIH.

Author contributions

Z.C., Q.Z., Z.L. and K.C. conceived and designed the project. Z.C. and Q.Z. performed the clinical 3T MRI and [¹⁸F]FDG PET and CT experiments in humans. Z.C. and Q.Z. performed the metabolic cages and [¹⁸F]FDG PET and CT experiments in rats. Z.C. and Y.F. performed the 7T small-animal MRI experiments in rats. Q.W., Z.Z. and C.W. helped with rat sampling, and the RT-qPCR and ¹H-NMR experiments. Z.C. and Q.Z. analysed the data and prepared the figures. Z.Y. and C.L. helped in conceiving the project, and mentored and supervised its participants. Z.C. and Q.Z. wrote the manuscript with help from C.W.L., L.K., A.M.C., Z.L. and K.C. C.W.L., L.K., A.M.C., Z.L. and K.C. helped in conceiving the project and provided guidance in the discussions.

Competing interests

K.C., Z.C. and Z.L. filed a US patent application through the University of Illinois at Chicago, ‘Systems and methods for magnetic resonance imaging (MRI) noninvasive mapping of brown adipose tissue activity’. The other authors declare no competing interests.

Additional information

Extended data is available for this paper at
<https://doi.org/10.1038/s42255-024-01082-z>.

Supplementary information The online version contains supplementary material available at
<https://doi.org/10.1038/s42255-024-01082-z>.

Correspondence and requests for materials should be addressed to Zaiyi Liu.

Peer review information *Nature Metabolism* thanks the anonymous reviewers for their contribution to the peer review of this work. Primary Handling Editor: Christoph Schmitt, in collaboration with the *Nature Metabolism* team.

Reprints and permissions information is available at
www.nature.com/reprints.

Publisher's note Springer Nature remains neutral with regard to jurisdictional claims in published maps and institutional affiliations.

Open Access This article is licensed under a Creative Commons Attribution 4.0 International License, which permits use, sharing, adaptation, distribution and reproduction in any medium or format, as long as you give appropriate credit to the original author(s) and the source, provide a link to the Creative Commons licence, and indicate if changes were made. The images or other third party material in this article are included in the article's Creative Commons licence, unless indicated otherwise in a credit line to the material. If material is not included in the article's Creative Commons licence and your intended use is not permitted by statutory regulation or exceeds the permitted use, you will need to obtain permission directly from the copyright holder. To view a copy of this licence, visit <http://creativecommons.org/licenses/by/4.0/>.

© The Author(s) 2024

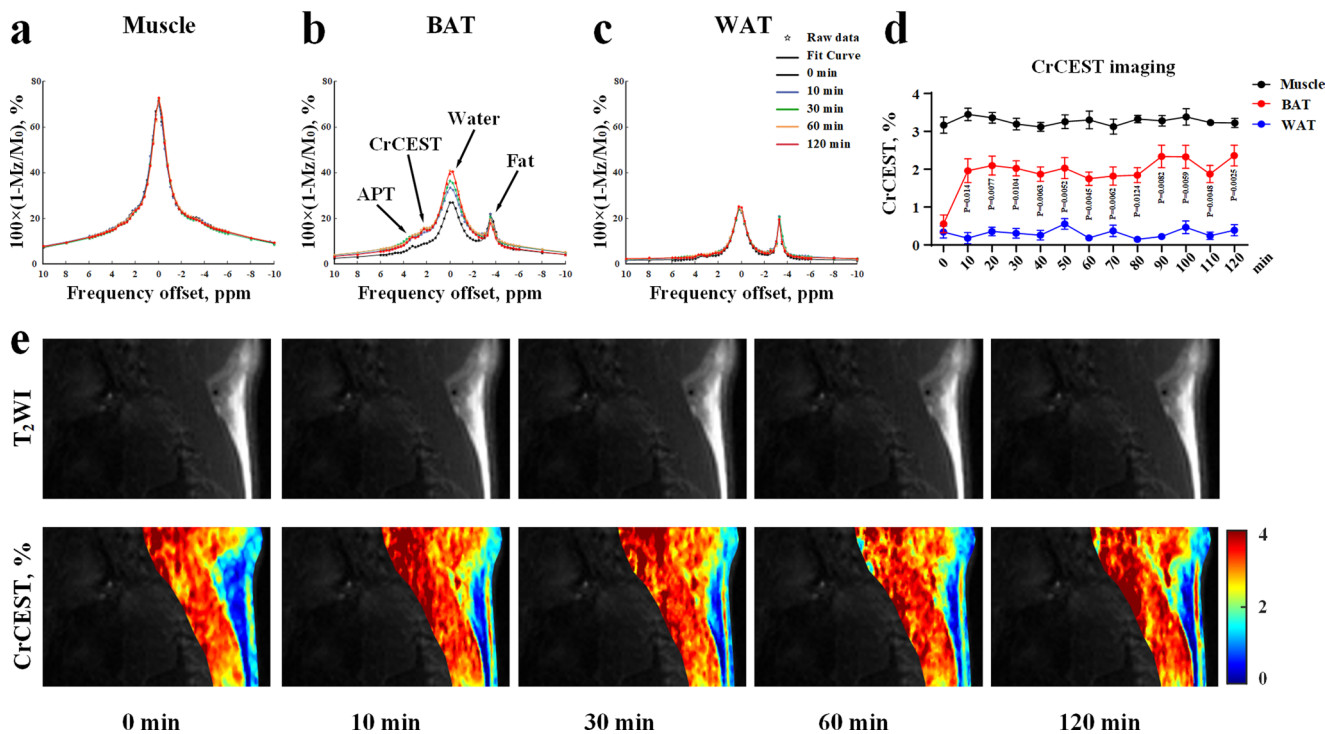
¹Department of Radiology, Guangdong Provincial People's Hospital (Guangdong Academy of Medical Sciences), Southern Medical University, Guangzhou, China. ²School of Medicine, South China University of Technology, Guangzhou, China. ³Guangdong Provincial Key Laboratory of Artificial Intelligence in Medical Image Analysis and Application, Guangzhou, China. ⁴Department of Radiology, Guangzhou Women and Children's Medical Center, Guangzhou Medical University, Guangzhou, China. ⁵School of Biomedical Engineering, Southern Medical University, Guangzhou, China.

⁶Guangdong Provincial Key Laboratory of Medical Image Processing & Guangdong Province Engineering Laboratory for Medical Imaging and Diagnostic Technology, Southern Medical University, Guangzhou, China. ⁷Guangdong-Hong Kong-Macao Greater Bay Area Center for Brain Science and Brain-Inspired Intelligence & Key Laboratory of Mental Health of the Ministry of Education, Southern Medical University, Guangzhou, China. ⁸The Biomedical Translational Research Institute, Faculty of Medical Science, Jinan University, Guangzhou, China. ⁹Department of Neonatology, Nanfang Hospital, Southern Medical University, Guangzhou, China. ¹⁰School of Medicine, Shenzhen Campus, Sun Yat-sen University, Shenzhen, China. ¹¹Guangdong Provincial Key Laboratory of Tumor Interventional Diagnosis and Treatment, Zhuhai Institute of Translational Medicine, Zhuhai People's Hospital Affiliated with Jinan University, Jinan University, Zhuhai, China. ¹²Physiology and Biophysics Department, University of Illinois at Chicago, Chicago, IL, USA.

¹³Rosalind & Morris Goodman Cancer Institute, McGill University, Montreal, Quebec, Canada. ¹⁴Department of Biochemistry, McGill University, Montreal, Quebec, Canada. ¹⁵Diabetes, Endocrinology, and Obesity Branch, Intramural Research Program, National Institute of Diabetes and Digestive and Kidney Diseases (NIDDK), National Institutes of Health, Bethesda, MD, USA. ¹⁶Department of Radiology, University of Illinois at Chicago, Chicago, IL, USA.

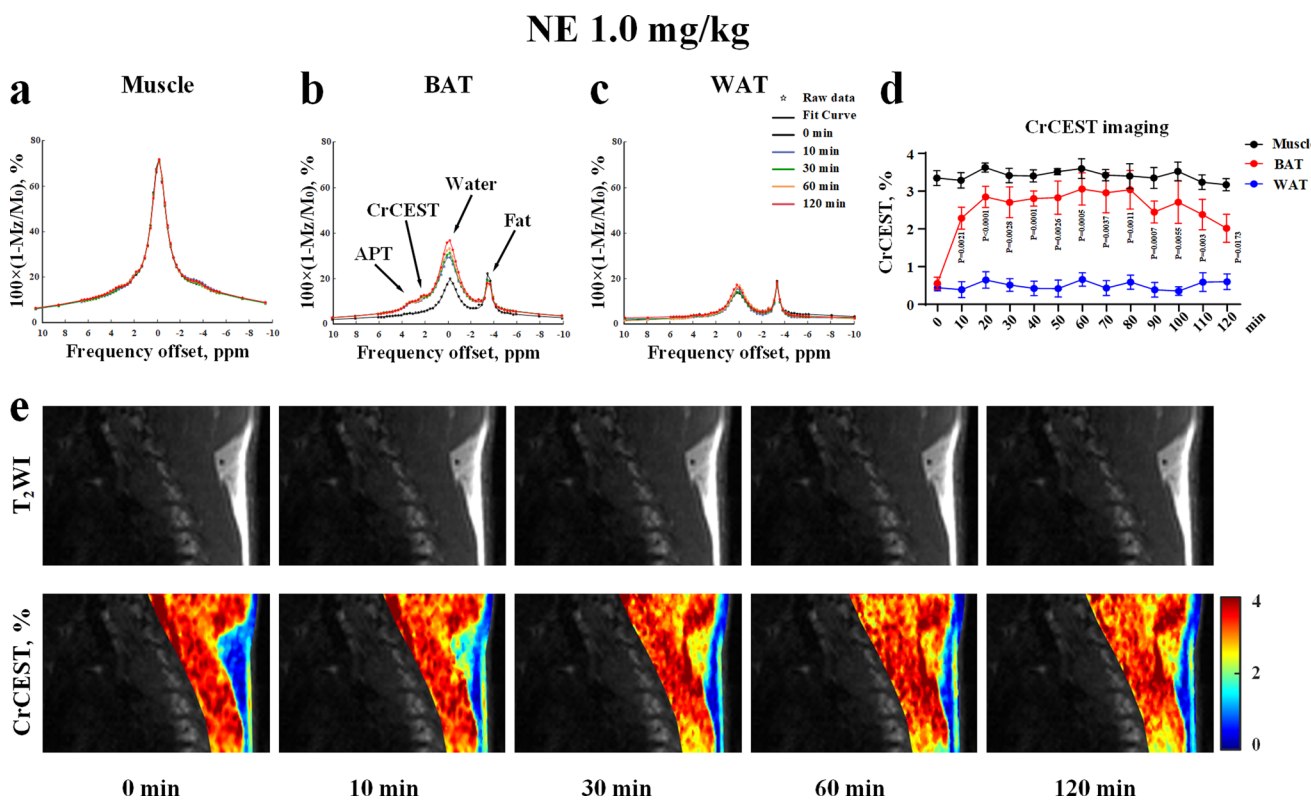
¹⁷Department of Biomedical Engineering, University of Illinois at Chicago, Chicago, IL, USA. ¹⁸These authors contributed equally: Zimeng Cai, Qiaoling Zhong, Yanqiu Feng, Qian Wang. ✉e-mail: liuzaiyi@gdph.org.cn

CL 316, 243 1.0 mg/kg



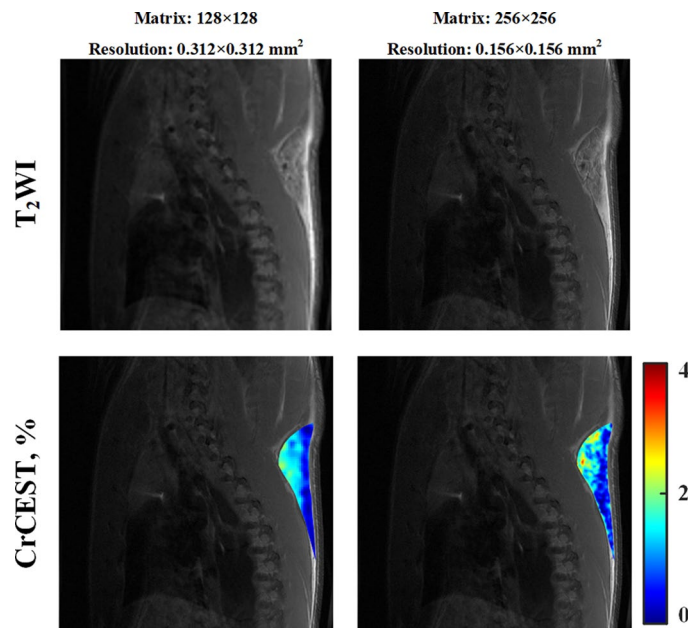
Extended Data Fig. 1 | Representative Z-spectra (a-c), CrCEST (d), and CrCEST maps (e) under CL 316, 243 stimulation for 2 hours in rats. Representative image (from $n = 6$). Data are presented as means \pm s.e.m., $n = 6$. When activated, the CrCEST signal of BAT increased, accompanied by the increase of water signal and the decrease of fat signal. Statistical analysis was performed using two-tailed

paired Student's t-tests, and each time point (10–120 min) was compared to 0 min (d), respectively. In Z-spectra, arrows were pointed to the water, fat, CrCEST, and APT peaks, respectively. Note that the area containing lung cavity is not shown due to sparse signal and artifacts.

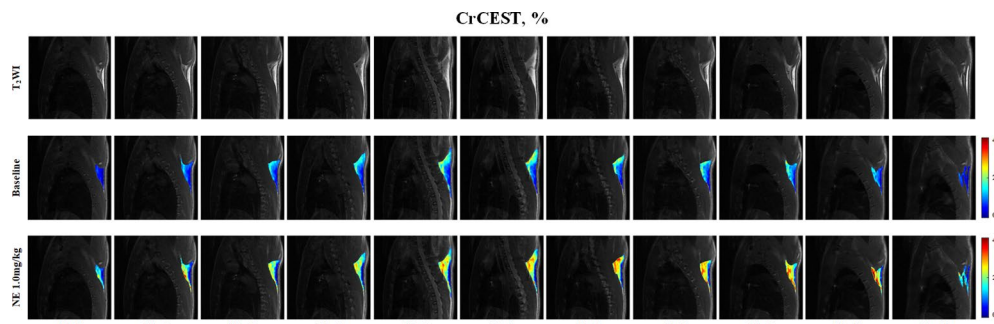


Extended Data Fig. 2 | Representative Z-spectra (a-c), CrCEST (d), and CrCEST maps (e) under NE stimulation for 2 hours in rats. Representative image (from $n = 6$). Data are presented as means \pm s.e.m., $n = 6$. When activated, the CrCEST signal of BAT increased, accompanied by the increase of water signal and the decrease of fat signal. Statistical analysis was performed using two-tailed paired

Student's t-tests, and each time point (10–120 min) was compared to 0 min (d) respectively. In Z-spectra, arrows were pointed to the water, fat, CrCEST, and APT peaks, respectively. Note that the area containing lung cavity is not shown due to sparse signal and artifacts.

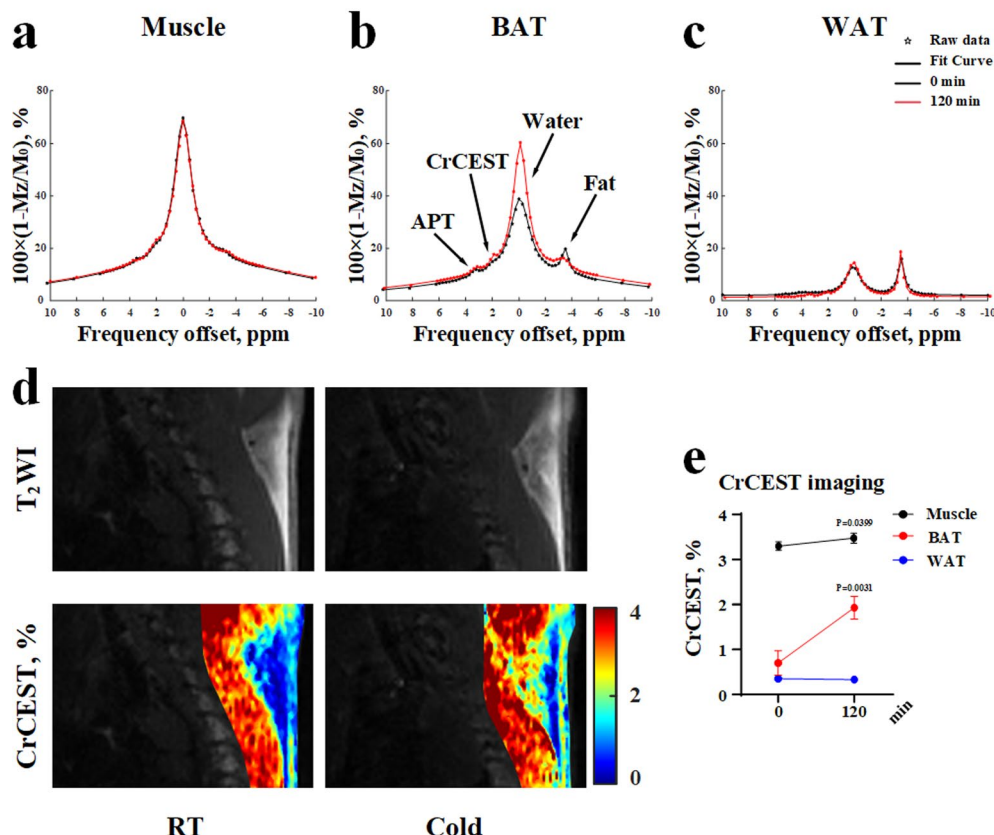


Extended Data Fig. 3 | CrCEST MRI at different spatial resolutions. Increasing the spatial resolution helps to reduce the partial volume effect, delineate tissue boundaries, and therefore differentiate different types of adipose tissues. However, a longer scan time is required (8 mins vs. 16 mins). Representative image (from n=3).



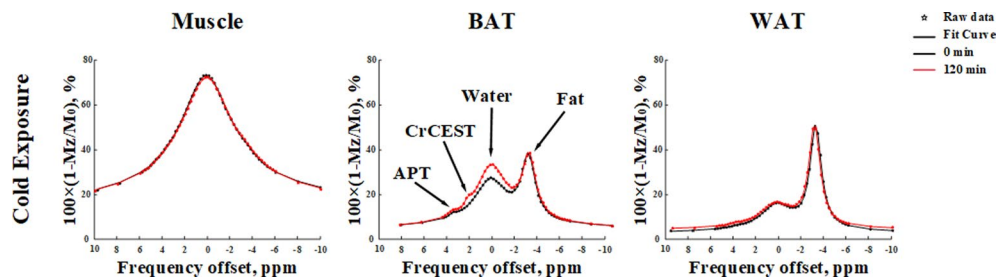
Extended Data Fig. 4 | Multi-slice CrCEST imaging of the entire interscapular fat depot 30-min post-injection of NE. The total scanning time is 14 mins. Representative image (from $n = 3$).

Cold Exposure

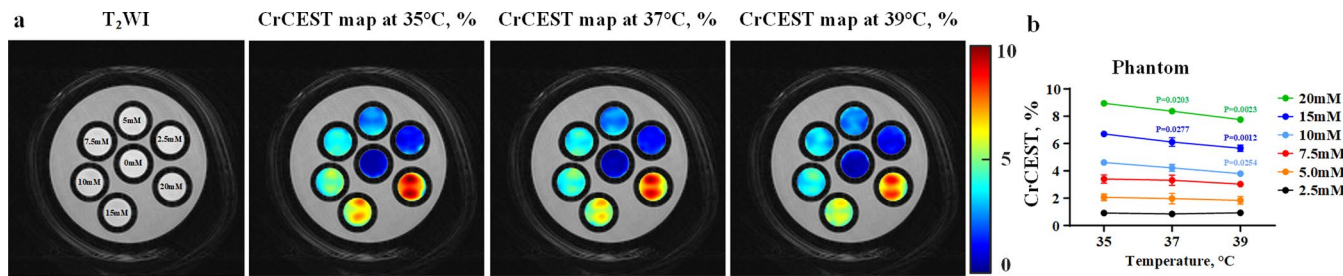


Extended Data Fig. 5 | Representative Z-spectra (a-c), CrCEST maps (d), and CrCEST (e) under room temperature (RT, 0 min) and 2-hour cold exposure in rats. Representative image (from $n=7$). Data are presented as means \pm s.e.m., $n=7$. When activated, the CrCEST signal of BAT increased, accompanied by the

increase of water signal and the decrease of fat signal. Statistical analysis was performed using two-tailed paired Student's t-tests (d). In Z-spectra, arrows were pointed to the water, fat, CrCEST, and APT peaks, respectively. Note that the area containing lung cavity is not shown due to sparse signal and artifacts.

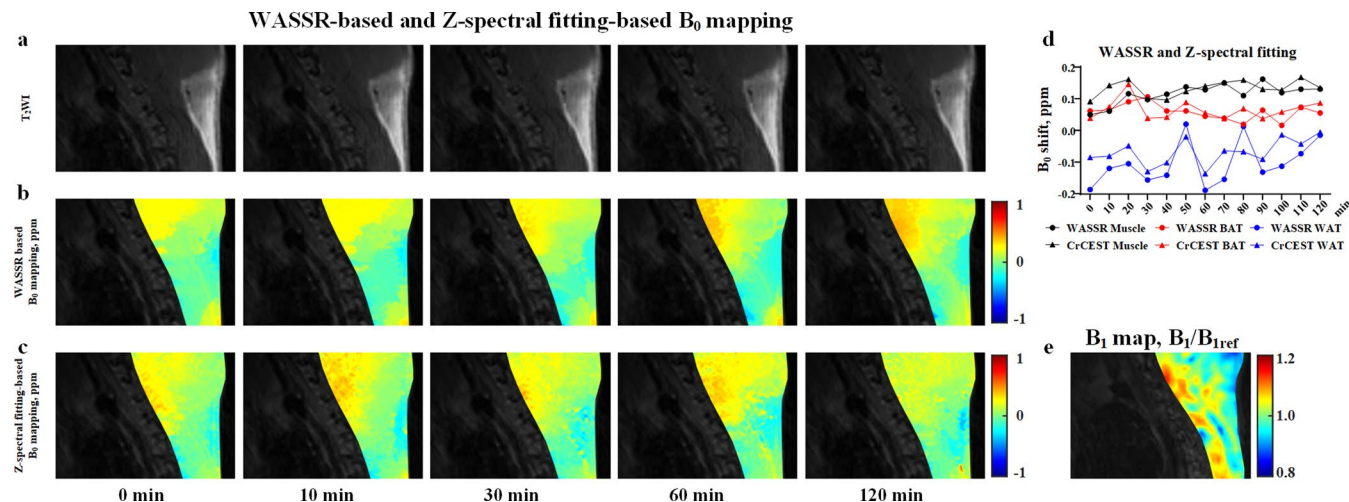


Extended Data Fig. 6 | Z-spectra under room temperature (RT, 0 min) and 2-hour cold exposure in humans. The CrCEST and water signals of BAT Z-spectra increased significantly after 2 hours mild-cold exposure. In Z-spectra, arrows were pointed to the water, fat, CrCEST, and APT peaks, respectively.



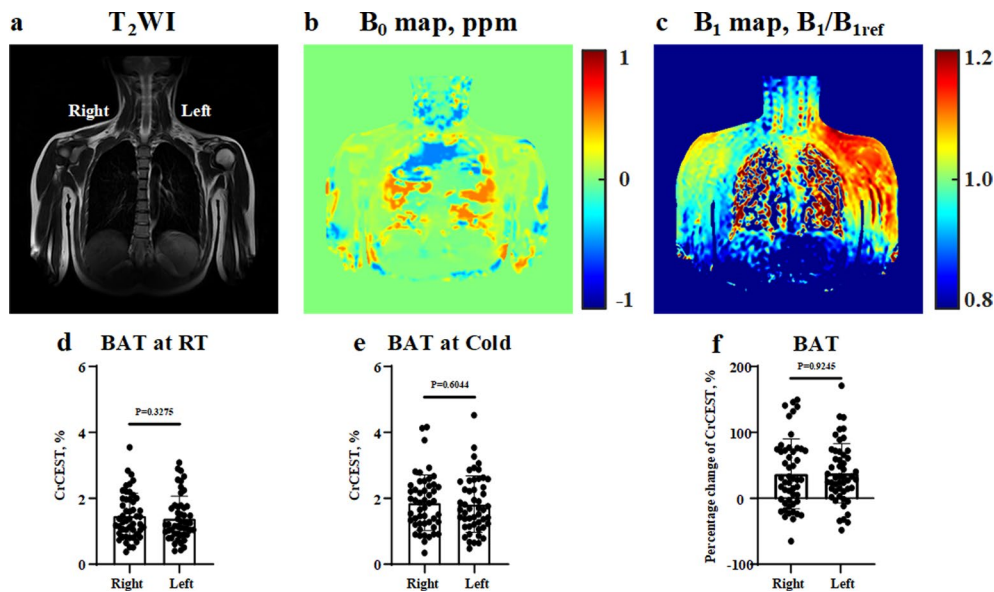
Extended Data Fig. 7 | CrCEST MRI of creatine solutions at different temperatures. Relationship between CrCEST and temperature for different creatine concentrations (2.5 mM, 5.0 mM, 7.5 mM, 10 mM, 15 mM, and 20 mM), n = 3. (a) T₂WI, and the CrCEST maps at different temperatures (35 °C, 37 °C, and 39 °C respectively). (b) When the concentration of creatine was equal to or higher

than 10 mM, the CrCEST signal showed a tendency to gradually decrease from 35 °C to 39 °C. Representative image (from n = 3). Data are presented as means ± s.d. Statistical analysis was performed using two-tailed paired Student's t-tests. Each temperature (37 and 39 °C) was compared to 35 °C.



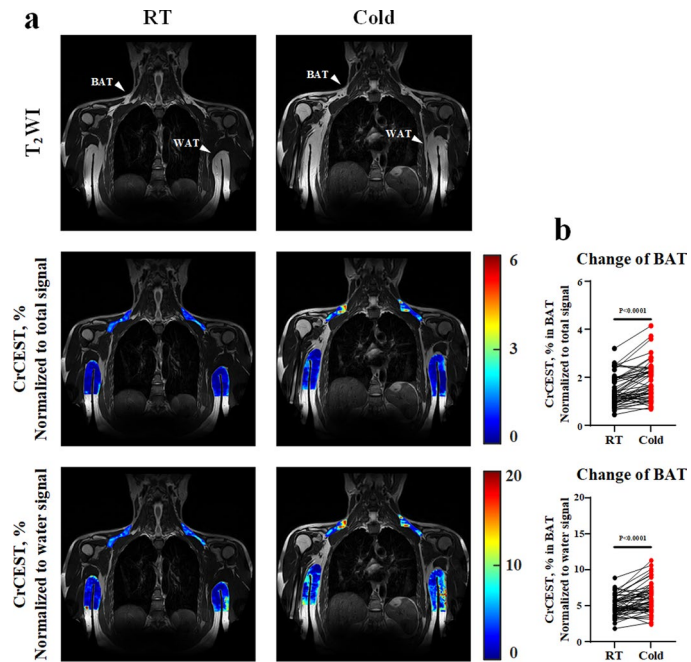
Extended Data Fig. 8 | B_0 and B_1 mapping of the interscapular fat depot in rats. (a-c) Dynamic B_0 mapping based on WASSR and Z-spectral fitting of fat depot before and post the injection of CL 316, 243 in rats, representative B_0 maps (from $n=3$). (d) The dynamics of WASSR-based and Z-spectral fitting-based B_0

shift in muscle, BAT, and WAT during the 2-hour CL 316, 243 stimulation. (e) A representative B_1 map of the interscapular fat depot in rats, representative B_1 map (from $n=3$). Note that the area containing lung cavity is not shown due to sparse signal and artifacts.



Extended Data Fig. 9 | B₀ and B₁ inhomogeneity of human subjects did not affect the results of CrCEST MRI at 3T. (a–c) The representative T₂WI and B₀ and the B₁ maps for the interscapular fat depot in human. **(d, e)** BAT CrCEST results showed no statistical differences between the left and right sides of the body before and after cold exposure (n = 50). **(f)** Percentage changes of CrCEST before

and after cold exposure showed no statistical differences between the left and right sides (n = 50). RT, room temperature. Representative image (from n = 50). Data are presented as means \pm s.d. Statistical analysis was performed using two-tailed paired Student's t-tests.



Extended Data Fig. 10 | Normalized CrCEST maps of human subjects before and after cold exposure. (a) Besides rescaling the values, CrCEST maps normalized to the water signal did not change the overall spatial pattern of BAT activation. (b) Both types of normalized CrCEST showed significantly increased

CrCEST due to cold exposure in humans. Statistical analysis was performed using two-tailed paired Student's t-tests, n = 50 (b). Representative image (from n = 50). RT, room temperature. In T₂WI, arrowheads were pointed to the BAT and WAT regions, respectively.

Corresponding author(s): Zaiyi Liu

Last updated by author(s): May 10, 2024

Reporting Summary

Nature Portfolio wishes to improve the reproducibility of the work that we publish. This form provides structure for consistency and transparency in reporting. For further information on Nature Portfolio policies, see our [Editorial Policies](#) and the [Editorial Policy Checklist](#).

Statistics

For all statistical analyses, confirm that the following items are present in the figure legend, table legend, main text, or Methods section.

n/a Confirmed

- The exact sample size (n) for each experimental group/condition, given as a discrete number and unit of measurement
- A statement on whether measurements were taken from distinct samples or whether the same sample was measured repeatedly
- The statistical test(s) used AND whether they are one- or two-sided
Only common tests should be described solely by name; describe more complex techniques in the Methods section.
- A description of all covariates tested
- A description of any assumptions or corrections, such as tests of normality and adjustment for multiple comparisons
- A full description of the statistical parameters including central tendency (e.g. means) or other basic estimates (e.g. regression coefficient) AND variation (e.g. standard deviation) or associated estimates of uncertainty (e.g. confidence intervals)
- For null hypothesis testing, the test statistic (e.g. F , t , r) with confidence intervals, effect sizes, degrees of freedom and P value noted
Give P values as exact values whenever suitable.
- For Bayesian analysis, information on the choice of priors and Markov chain Monte Carlo settings
- For hierarchical and complex designs, identification of the appropriate level for tests and full reporting of outcomes
- Estimates of effect sizes (e.g. Cohen's d , Pearson's r), indicating how they were calculated

Our web collection on [statistics for biologists](#) contains articles on many of the points above.

Software and code

Policy information about [availability of computer code](#)

Data collection

- Male rat MRI experiments were performed using a 7T small-bore MRI scanner (Bruker Biospec, Billerica, MA, USA).
- MRI-compatible small animal-monitoring system (Small Animal Instruments, Stony Brook, NY, USA)
- Male rat 18F-FDG PET/CT experiments were performed using a Micro-PET/CT system (IRIS PET/CT, Invacan, Strasbourg, France).
- Small-animal-monitoring system (Equipement Veterinaire Minerve, Esternay, France).
- Human MRI imaging was performed with a 3T whole-body MRI scanner (Ingenia CX, Philips Healthcare, Best, the Netherlands).
- Human 18F-FDG PET/CT imaging was performed with a Biograph mCT Flow 64 PET/CT system (Siemens Healthcare, Erlangen, Germany).
- Quantitative PCR was performed with the CFX96 Real-Time PCR Detection System (Bio-Rad Laboratories, Inc, Hercules, California, USA).
- The 1H-NMR spectra were acquired using a Bruker 600 MHz Avance III HD spectrometer (Bruker Biospec, Billerica, MA, USA).
- Promethion high-definition behavioral phenotyping system (Sable Systems International, Las Vegas, NV, USA).

Data analysis

- GraphPad Prism (v.8.3.0); Sable Systems International Macro Interpreter software (v.22.10); One-Click Macro (v2.51.4); MestReNova (V14.0, Mestrelab Research, Spain) software; MATLAB (R2020a, MathWorks, Natick, MA).

For manuscripts utilizing custom algorithms or software that are central to the research but not yet described in published literature, software must be made available to editors and reviewers. We strongly encourage code deposition in a community repository (e.g. GitHub). See the Nature Portfolio [guidelines for submitting code & software](#) for further information.

Data

Policy information about [availability of data](#)

All manuscripts must include a [data availability statement](#). This statement should provide the following information, where applicable:

- Accession codes, unique identifiers, or web links for publicly available datasets
- A description of any restrictions on data availability
- For clinical datasets or third party data, please ensure that the statement adheres to our [policy](#)

All source data are provided as supplementary information.

Human research participants

Policy information about [studies involving human research participants](#) and [Sex and Gender in Research](#).

Reporting on sex and gender	Twenty-seven male and twenty-three female volunteers were equally included based on willingness to participate in this study.
Population characteristics	Fifty young and healthy volunteers (27 male, 23 female, Age: 22.42 ± 1.85 , BMI: 21.31 ± 3.51 , mean \pm s.d) were recruited in this study.
Recruitment	The healthy volunteers were recruited using the call for trial participation by the group chat of Southern Medical University. No self-selection bias during the recruitment in this study.
Ethics oversight	Informed consent was obtained from all participants. All human studies were approved by the Ethical Review Committee in the Guangdong Provincial People's Hospital, China.

Note that full information on the approval of the study protocol must also be provided in the manuscript.

Field-specific reporting

Please select the one below that is the best fit for your research. If you are not sure, read the appropriate sections before making your selection.

Life sciences Behavioural & social sciences Ecological, evolutionary & environmental sciences

For a reference copy of the document with all sections, see nature.com/documents/nr-reporting-summary-flat.pdf

Life sciences study design

All studies must disclose on these points even when the disclosure is negative.

Sample size	No sample size predetermination was performed. The sample size was chosen based on previous experience to achieve statistical significance.
Data exclusions	No data were excluded.
Replication	All experiments have been successfully replicated showing the same results for at least three times.
Randomization	All subjects were randomly allocated into the study groups.
Blinding	All experimental data were reviewed blind by at least two independent researchers.

Reporting for specific materials, systems and methods

We require information from authors about some types of materials, experimental systems and methods used in many studies. Here, indicate whether each material, system or method listed is relevant to your study. If you are not sure if a list item applies to your research, read the appropriate section before selecting a response.

Materials & experimental systems

n/a	Involved in the study
<input checked="" type="checkbox"/>	Antibodies
<input checked="" type="checkbox"/>	Eukaryotic cell lines
<input checked="" type="checkbox"/>	Palaeontology and archaeology
<input type="checkbox"/>	Animals and other organisms
<input type="checkbox"/>	Clinical data
<input checked="" type="checkbox"/>	Dual use research of concern

Methods

n/a	Involved in the study
<input checked="" type="checkbox"/>	ChIP-seq
<input checked="" type="checkbox"/>	Flow cytometry
<input checked="" type="checkbox"/>	MRI-based neuroimaging

Animals and other research organisms

Policy information about [studies involving animals; ARRIVE guidelines](#) recommended for reporting animal research, and [Sex and Gender in Research](#)

Laboratory animals	Sprague Dawley rats, male, age 8 weeks.
Wild animals	The study did not use wild animals.
Reporting on sex	This initial technological development is not expected to be gender-related. In addition, obesity is common in both male and female.
Field-collected samples	The study did not use field-collected samples.
Ethics oversight	All animal experiments were approved by the Institutional Animal Use and Care Committee of Guangdong Provincial People's Hospital.

Note that full information on the approval of the study protocol must also be provided in the manuscript.

Clinical data

Policy information about [clinical studies](#)

All manuscripts should comply with the ICMJE [guidelines for publication of clinical research](#) and a completed [CONSORT checklist](#) must be included with all submissions.

Clinical trial registration	Not applicable.
Study protocol	Proof-of-concept and technical-development study.
Data collection	All the healthy volunteers were recruited from September 2021 to January 2024 at Southern Medical University in this study. All the information about human participants has been provided in the manuscript.
Outcomes	Not applicable.